

Central Lancashire Online Knowledge (CLOK)

Title	Polarimetric Geometric Modeling for mm-VLBI Observations of Black Holes
Type	Article
URL	https://clock.uclan.ac.uk/49599/
DOI	##doi##
Date	2023
Citation	Roelofs, Freek, Johnson, Michael D., Chael, Andrew, Janssen, Michael, Wielgus, Maciek, Broderick, Avery E., Akiyama, Kazunori, Alberdi, Antxon, Alef, Walter et al (2023) Polarimetric Geometric Modeling for mm-VLBI Observations of Black Holes. <i>Astrophysical Journal Letters</i> , 957 (2). ISSN 2041-8205
Creators	Roelofs, Freek, Johnson, Michael D., Chael, Andrew, Janssen, Michael, Wielgus, Maciek, Broderick, Avery E., Akiyama, Kazunori, Alberdi, Antxon, Alef, Walter, Algaba, Juan Carlos, Anantua, Richard, Asada, Keiichi, Azulay, Rebecca, Bach, Uwe, Baczko, Anne-Kathrin, Ball, David, Baloković, Mislav, Barrett, John, Bauböck, Michi, Benson, Bradford A., Bintley, Dan, Blackburn, Lindy, Blundell, Raymond, Bouman, Katherine L., Bower, Geoffrey C., Boyce, Hope, Bremer, Michael, Brinkerink, Christiaan D., Brissenden, Roger, Britzen, Silke, Broguiere, Dominique, Bronzwaer, Thomas, Bustamante, Sandra, Byun, Do-Young, Carlstrom, John E., Ceccobello, Chiara, Chan, Chikwan, Chang, Dominic O., Chatterjee, Koushik, Chatterjee, Shami, Chen, Ming-Tang, Chen, Yongjun, Cheng, Xiaopeng, Cho, Ilje, Christian, Pierre, Conroy, Nicholas S., Conway, John E., Cordes, James M., Crawford, Thomas M., Crew, Geoffrey B., Cruz-Osorio, Alejandro, Cui, Yuzhu, Dahale, Rohan, Davelaar, Jordy, De Laurentis, Mariafelicia, Deane, Roger, Dempsey, Jessica, Desvignes, Gregory, Dexter, Jason, Dhruv, Vedant, Doeleman, Sheperd S., Dougal, Sean, Dzib, Sergio A., Eatough, Ralph P., Emami, Razieh, Falcke, Heino, Farah, Joseph, Fish, Vincent L., Fomalont, Ed, Ford, H. Alyson, Foschi, Marianna, Fraga-Encinas, Raquel, Freeman, William T., Friberg, Per, Fromm, Christian M., Fuentes, Antonio, Galison, Peter, Gammie, Charles F., García, Roberto, Gentaz, Olivier, Georgiev, Boris, Goddi, Ciriaco, Gold, Roman, Gómez-Ruiz, Arturo I., Gómez, José L., Gu, Minfeng, Gurwell, Mark, Hada, Kazuhiro, Haggard, Daryl, Haworth, Kari, Hecht, Michael H., Hesper, Ronald, Heumann, Dirk, Ho, Luis C., Ho, Paul, Honma, Mareki, Huang, Chih-Wei L., Huang, Lei, Hughes, David H., Ikeda, Shiro, Impellizzeri, C. M. Violette, Inoue, Makoto, Issaoun, Sara, James, David J., Jannuzi, Buell T., Jeter, Britton, Jiang, Wu, Jiménez-Rosales, Alejandra, Jorstad, Svetlana, Joshi, Abhishek V., Jung, Taehyun, Karami, Mansour, Karuppusamy, Ramesh, Kawashima, Tomohisa, Keating, Garrett K., Kettenis, Mark, Kim, Dong-Jin, Kim, Jae-Young, Kim, Jongsoo, Kim, Junhan, Kino, Motoki, Koay, Jun Yi, Kocherlakota, Prashant, Kofuji, Yutaro, Koch, Patrick M., Koyama, Shoko, Kramer, Carsten, Kramer, Joana A., Kramer, Michael, Krichbaum, Thomas P., Kuo, Cheng-Yu, La Bella, Noemi, Lauer, Tod R., Lee, Daeyoung, Lee, Sang-Sung, Leung, Po Kin, Levis, Aviad, Li, Zhiyuan, Lico, Rocco, Lindahl, Greg, Lindqvist, Michael, Lisakov, Mikhail, Liu, Jun, Liu, Kuo, Liuzzo, Elisabetta, Lo, Wen-Ping, Lobanov, Andrei P., Loinard, Laurent, Lonsdale, Colin J., Lowitz, Amy E., Lu, Ru-Sen, MacDonald, Nicholas R., Mao, Jirong, Marchili, Nicola, Markoff, Sera, Marrone, Daniel P., Marscher, Alan P., Martí-Vidal, Iván, Matsushita, Satoki, Matthews, Lynn D., Medeiros, Lia, Menten, Karl M., Michalik, Daniel, Mizuno, Izumi, Mizuno, Yosuke, Moran, James M., Moriyama, Kotaro, Moscibrodzka, Monika, Mulaudzi, Wanga, Müller, Cornelia, Müller, Hendrik, Mus, Alejandro, Musoke, Gibwa, Myserlis, Ioannis, Nadolski, Andrew, Nagai, Hiroshi, Nagar,

	<p>Neil M., Nakamura, Masanori, Narayanan, Gopal, Natarajan, Iniyan, Nathanail, Antonios, Fuentes, Santiago Navarro, Neilsen, Joey, Neri, Roberto, Ni, Chunchong, Noutsos, Aristeidis, Nowak, Michael A., Oh, Junghwan, Okino, Hiroki, Olivares, Héctor, Ortiz-León, Gisela N., Oyama, Tomoaki, Özel, Feryal, Palumbo, Daniel C. M., Paraschos, Georgios Filippou, Park, Jongho, Parsons, Harriet, Patel, Nimesh, Pen, Ue-Li, Pesce, Dominic W., Piétu, Vincent, Plambeck, Richard, PopStefanija, Aleksandar, Porth, Oliver, Pötzl, Felix M., Prather, Ben, Preciado-López, Jorge A., Psaltis, Dimitrios, Pu, Hung-Yi, Ramakrishnan, Venkatesh, Rao, Ramprasad, Rawlings, Mark G., Raymond, Alexander W., Rezzolla, Luciano, Ricarte, Angelo, Ripperda, Bart, Rogers, Alan, Romero-Cañizales, Cristina, Ros, Eduardo, Roshanineshat, Arash, Rottmann, Helge, Roy, Alan L., Ruiz, Ignacio, Ruzsczyk, Chet, Rygl, Kazi L. J., Sánchez, Salvador, Sánchez-Argüelles, David, Sánchez-Portal, Miguel, Sasada, Mahito, Satapathy, Kaushik, Savolainen, Tuomas, Schloerb, F. Peter, Schonfeld, Jonathan, Schuster, Karl-Friedrich, Shao, Lijing, Shen, Zhiqiang, Small, Des, Sohn, Bong Won, SooHoo, Jason, Sosapanta Salas, León David, Souccar, Kamal, Sun, He, Tazaki, Fumie, Tetarenko, Alexandra J., Tiede, Paul, Tilanus, Remo P. J., Titus, Michael, Torne, Pablo, Toscano, Teresa, Traianou, Efthalia, Trent, Tyler, Trippe, Sascha, Turk, Matthew, van Bommel, Ilse, van Langevelde, Huib Jan, van Rossum, Daniel R., Vos, Jesse, Wagner, Jan, Ward-Thompson, Derek, Wardle, John, Washington, Jasmin E., Weintraub, Jonathan, Wharton, Robert, Wiik, Kaj, Witzel, Gunther, Wondrak, Michael F., Wong, George N., Wu, Qingwen, Yadlapalli, Nitika, Yamaguchi, Paul, Yfantis, Aristomenis, Yoon, Doosoo, Young, André, Young, Ken, Younsi, Ziri, Yu, Wei, Yuan, Feng, Yuan, Ye-Fei, Zensus, J. Anton, Zhang, Shuo, Zhao, Guang-Yao and Zhao, Shan-Shan</p>
--	---

It is advisable to refer to the publisher's version if you intend to cite from the work. ##doi##







For information about Research at UCLan please go to <http://www.uclan.ac.uk/research/>

All outputs in CLoK are protected by Intellectual Property Rights law, including Copyright law. Copyright, IPR and Moral Rights for the works on this site are retained by the individual authors and/or other copyright owners. Terms and conditions for use of this material are defined in the <http://cllok.uclan.ac.uk/policies/>



Polarimetric Geometric Modeling for mm-VLBI Observations of Black Holes

Freek Roelofs^{1,2,3} , Michael D. Johnson^{1,2} , Andrew Chael⁴ , Michael Janssen⁵ , Maciek Wielgus⁵ ,
 Avery E. Broderick^{6,7,8} , Kazunori Akiyama^{9,10,11} , Antxon Alberdi¹² , Walter Alef⁵ , Juan Carlos Algaba¹³ ,
 Richard Anantua^{11,1,14} , Keiichi Asada¹⁵ , Rebecca Azulay^{16,17,5} , Uwe Bach⁵ , Anne-Kathrin Baczko^{18,5} , David Ball¹⁹ ,
 Mislav Baloković²⁰ , John Barrett⁹ , Michi Bauböck²¹ , Bradford A. Benson^{22,23} , Dan Bintley^{24,25} , Lindy Blackburn^{11,1} ,
 Raymond Blundell¹ , Katherine L. Bouman²⁶ , Geoffrey C. Bower^{27,28} , Hope Boyce^{29,30} , Michael Bremer³¹ ,
 Christiaan D. Brinkerink³ , Roger Brissenden^{11,1} , Silke Britzen⁵ , Dominique Brogiere³¹ , Thomas Bronzwaer³ ,
 Sandra Bustamante³² , Do-Young Byun^{33,34} , John E. Carlstrom^{35,23,36,37} , Chiara Ceccobello¹⁸ , Chi-kwan Chan^{19,38,39} ,
 Dominic O. Chang^{11,1} , Koushik Chatterjee^{11,1} , Shami Chatterjee⁴⁰ , Ming-Tang Chen²⁷ , Yongjun Chen (陈永军)^{41,42} ,
 Xiaopeng Cheng³³ , Ilje Cho¹² , Pierre Christian⁴³ , Nicholas S. Conroy^{44,1} , John E. Conway¹⁸ , James M. Cordes⁴⁰ ,
 Thomas M. Crawford^{23,35} , Geoffrey B. Crew⁹ , Alejandro Cruz-Osorio^{45,46} , Yuzhu Cui (崔玉竹)^{47,48} , Rohan Dahale¹² ,
 Jordy Davelaar^{49,50,3} , Mariafelicia De Laurentis^{51,46,52} , Roger Deane^{53,54,55} , Jessica Dempsey^{24,25,56} ,
 Gregory Desvignes^{5,57} , Jason Dexter⁵⁸ , Vedant Dhruv²¹ , Sheperd S. Doeleman^{11,1} , Sean Dougal¹⁹ ,
 Sergio A. Dzib^{31,5} , Ralph P. Eatough^{59,5} , Raziieh Emami¹ , Heino Falcke³ , Joseph Farah^{60,61} , Vincent L. Fish⁹ ,
 Ed Fomalont⁶² , H. Alyson Ford¹⁹ , Marianna Foschi¹² , Raquel Fraga-Encinas³ , William T. Freeman^{63,64} ,
 Per Friberg^{24,25} , Christian M. Fromm^{65,46,5} , Antonio Fuentes¹² , Peter Galison^{11,66,67} , Charles F. Gammie^{21,44,68} ,
 Roberto García³¹ , Olivier Gentaz³¹ , Boris Georgiev^{6,7,8} , Ciriaco Goddi^{69,70,71,72} , Roman Gold⁷³ ,
 Arturo I. Gómez-Ruiz^{74,75} , José L. Gómez¹² , Minfeng Gu (顾敏峰)^{41,76} , Mark Gurwell¹ , Kazuhiro Hada^{77,78} ,
 Daryl Haggard^{29,30} , Kari Haworth¹ , Michael H. Hecht⁹ , Ronald Hesper⁷⁹ , Dirk Heumann¹⁹ , Luis C. Ho (何子山)^{80,81} ,
 Paul Ho^{15,25,24} , Mareki Honma^{77,78,82} , Chih-Wei L. Huang¹⁵ , Lei Huang (黄磊)^{41,76} , David H. Hughes⁷⁴ ,
 Shiro Ikeda^{10,83,84,85} , C. M. Violette Impellizzeri^{86,62} , Makoto Inoue¹⁵ , Sara Issaoun^{1,155} , David J. James^{87,88} ,
 Buell T. Jannuzi¹⁹ , Britton Jeter¹⁵ , Wu Jiang (江悟)⁴¹ , Alejandra Jiménez-Rosales³ , Svetlana Jorstad⁸⁹ ,
 Abhishek V. Joshi²¹ , Taehyun Jung^{33,34} , Mansour Karami^{6,7} , Ramesh Karuppusamy⁵ , Tomohisa Kawashima⁹⁰ ,
 Garrett K. Keating¹ , Mark Kettenis⁹¹ , Dong-Jin Kim⁵ , Jae-Young Kim^{92,5} , Jongsoo Kim³³ , Junhan Kim²⁶ ,
 Motoki Kino^{10,93} , Jun Yi Koay¹⁵ , Prashant Kocherlakota⁴⁶ , Yutaro Kofuji^{77,82} , Patrick M. Koch¹⁵ , Shoko Koyama^{94,15} ,
 Carsten Kramer³¹ , Joana A. Kramer⁵ , Michael Kramer⁵ , Thomas P. Krichbaum⁵ , Cheng-Yu Kuo^{95,15} ,
 Noemi La Bella³ , Tod R. Lauer⁹⁶ , Daeyoung Lee²¹ , Sang-Sung Lee³³ , Po Kin Leung⁹⁷ , Aviad Levis²⁶ , Zhiyuan Li
 (李志远)^{98,99} , Rocco Lico^{100,12} , Greg Lindahl¹ , Michael Lindqvist¹⁸ , Mikhail Lisakov⁵ , Jun Liu (刘俊)⁵ ,
 Kuo Liu⁵ , Elisabetta Liuzzo¹⁰¹ , Wen-Ping Lo^{15,102} , Andrei P. Lobanov⁵ , Laurent Loinard^{103,45} , Colin J. Lonsdale⁹ ,
 Amy E. Lowitz¹⁹ , Ru-Sen Lu (路如森)^{42,5,41} , Nicholas R. MacDonald⁵ , Jirong Mao (毛基荣)^{104,105,106} ,
 Nicola Marchili^{101,5} , Sera Markoff^{107,108} , Daniel P. Marrone¹⁹ , Alan P. Marscher⁸⁹ , Iván Martí-Vidal^{16,17} ,
 Satoki Matsushita¹⁵ , Lynn D. Matthews⁹ , Lia Medeiros^{155,109} , Karl M. Menten⁵ , Daniel Michalik^{110,23} ,
 Izumi Mizuno^{24,25} , Yosuke Mizuno^{48,111,46} , James M. Moran^{11,1} , Kotaro Moriyama^{46,9,77} , Monika Moscibrodzka³ ,
 Wanga Mulaudzi¹⁰⁷ , Cornelia Müller^{5,3} , Hendrik Müller⁵ , Alejandro Mus^{16,17} , Gibwa Musoke^{107,3} ,
 Ioannis Myserlis¹¹² , Andrew Nadolski⁴⁴ , Hiroshi Nagai^{10,78} , Neil M. Nagar¹¹³ , Masanori Nakamura^{114,15} ,
 Gopal Narayanan³² , Iniyar Natarajan^{1,11} , Antonios Nathanail^{115,46} , Santiago Navarro Fuentes¹¹² , Joey Neilsen¹¹⁶ ,
 Roberto Neri³¹ , Chunchong Ni^{6,7,8} , Aristeidis Noutsos⁵ , Michael A. Nowak¹¹⁷ , Junghwan Oh¹¹⁸ , Hiroki Okino^{77,82} ,
 Héctor Olivares³ , Gisela N. Ortiz-León^{74,5} , Tomoaki Oyama⁷⁷ , Feryal Özel¹¹⁹ , Daniel C. M. Palumbo^{11,1} ,
 Georgios Filippou Paraschos⁵ , Jongho Park¹²⁰ , Harriet Parsons^{24,25} , Nimesh Patel¹ , Ue-Li Pen^{15,6,121,122,123} ,
 Dominic W. Pesce^{1,11} , Vincent Piétu³¹ , Richard Plambeck¹²⁴ , Aleksandar PopStefanija³² , Oliver Porth^{107,46} ,
 Felix M. Pötzl^{125,5} , Ben Prather²¹ , Jorge A. Preciado-López⁶ , Dimitrios Psaltis¹¹⁹ , Hung-Yi Pu^{126,127,15} ,
 Venkatesh Ramakrishnan^{113,128,129} , Ramprasad Rao¹ , Mark G. Rawlings^{130,24,25} , Alexander W. Raymond^{11,1} ,
 Luciano Rezzolla^{46,131,132} , Angelo Ricarte^{1,11} , Bart Ripperda^{121,133,122,6} , Alan Rogers⁹ , Cristina Romero-Cañizales¹⁵ ,
 Eduardo Ros⁵ , Arash Roshanineshat¹⁹ , Helge Rottmann⁵ , Alan L. Roy⁵ , Ignacio Ruiz¹¹² , Chet Ruszczyk⁹ ,
 Kazi L. J. Rygl¹⁰¹ , Salvador Sánchez¹¹² , David Sánchez-Argüelles^{74,75} , Miguel Sánchez-Portal¹¹² ,
 Mahito Sasada^{134,77,135} , Kaushik Satapathy¹⁹ , Tuomas Savolainen^{136,129,5} , F. Peter Schloerb³² , Jonathan Schonfeld¹ ,
 Karl-Friedrich Schuster³¹ , Lijing Shao^{81,5} , Zhiqiang Shen (沈志强)^{41,42} , Des Small⁹¹ , Bong Won Sohn^{33,34,137} ,
 Jason SooHoo⁹ , León David Sosapanta Salas¹⁰⁷ , Kamal Souccar³² , He Sun (孙赫)^{138,139} , Fumie Tazaki⁷⁷ ,
 Alexandra J. Tetarenko¹⁴⁰ , Paul Tiede^{1,11} , Remo P. J. Tilanus^{19,3,86,141} , Michael Titus⁹ , Pablo Torne^{112,5} ,
 Teresa Toscano¹² , Efthalia Traianou^{12,5} , Tyler Trent¹⁹ , Sascha Trippe¹⁴² , Matthew Turk⁴⁴ , Ilse van Bemmel⁹¹ ,
 Huib Jan van Langevelde^{91,86,143} , Daniel R. van Rossum³ , Jesse Vos³ , Jan Wagner⁵ , Derek Ward-Thompson¹⁴⁴ ,
 John Wardle¹⁴⁵ , Jasmin E. Washington¹⁹ , Jonathan Weintraub^{11,1} , Robert Wharton⁵ , Kaj Wiik¹⁴⁶ , Gunther Witzel⁵ ,
 Michael F. Wondrak^{3,147} , George N. Wong^{148,149} , Qingwen Wu (吴庆文)¹⁵⁰ , Nitika Yadlapalli²⁶ , Paul Yamaguchi¹ ,
 Aristomenis Yfantis³ , Doosoo Yoon¹⁰⁷ , André Young³ , Ken Young¹ , Ziri Younsi^{151,46} , Wei Yu (于威)¹ ,

Feng Yuan (袁峰)^{41,76,152} , Ye-Fei Yuan (袁业飞)¹⁵³ , J. Anton Zensus⁵ , Shuo Zhang¹⁵⁴ , Guang-Yao Zhao¹² , and
Shan-Shan Zhao (赵彬彬)⁴¹ 

¹ Center for Astrophysics | Harvard & Smithsonian, 60 Garden Street, Cambridge, MA 02138, USA; freek.roelofs@cfa.harvard.edu

² Black Hole Initiative, Harvard University, 20 Garden Street, Cambridge, MA 02138, USA

³ Department of Astrophysics, Institute for Mathematics, Astrophysics and Particle Physics (IMAPP), Radboud University, P.O. Box 9010, 6500 GL Nijmegen, The Netherlands

⁴ Princeton Gravity Initiative, Princeton University, Jadwin Hall, Princeton, NJ 08544, USA

⁵ Max-Planck-Institut für Radioastronomie, Auf dem Hügel 69, D-53121 Bonn, Germany

⁶ Perimeter Institute for Theoretical Physics, 31 Caroline Street North, Waterloo, ON, N2L 2Y5, Canada

⁷ Department of Physics and Astronomy, University of Waterloo, 200 University Avenue West, Waterloo, ON, N2L 3G1, Canada

⁸ Waterloo Centre for Astrophysics, University of Waterloo, Waterloo, ON, N2L 3G1, Canada

⁹ Massachusetts Institute of Technology Haystack Observatory, 99 Millstone Road, Westford, MA 01886, USA

¹⁰ National Astronomical Observatory of Japan, 2-21-1 Osawa, Mitaka, Tokyo 181-8588, Japan

¹¹ Black Hole Initiative at Harvard University, 20 Garden Street, Cambridge, MA 02138, USA

¹² Instituto de Astrofísica de Andalucía-CSIC, Glorieta de la Astronomía s/n, E-18008 Granada, Spain

¹³ Department of Physics, Faculty of Science, Universiti Malaya, 50603 Kuala Lumpur, Malaysia

¹⁴ Department of Physics & Astronomy, The University of Texas at San Antonio, One UTSA Circle, San Antonio, TX 78249, USA

¹⁵ Institute of Astronomy and Astrophysics, Academia Sinica, 11F of Astronomy-Mathematics Building, AS/NTU No. 1, Sec. 4, Roosevelt Rd., Taipei 10617, Taiwan, R.O.C.

¹⁶ Departament d'Astronomia i Astrofísica, Universitat de València, C. Dr. Moliner 50, E-46100 Burjassot, València, Spain

¹⁷ Observatori Astronòmic, Universitat de València, C. Catedrático José Beltrán 2, E-46980 Paterna, València, Spain

¹⁸ Department of Space, Earth and Environment, Chalmers University of Technology, Onsala Space Observatory, SE-43992 Onsala, Sweden

¹⁹ Steward Observatory and Department of Astronomy, University of Arizona, 933 N. Cherry Ave., Tucson, AZ 85721, USA

²⁰ Yale Center for Astronomy & Astrophysics, Yale University, 52 Hillhouse Avenue, New Haven, CT 06511, USA

²¹ Department of Physics, University of Illinois, 1110 West Green Street, Urbana, IL 61801, USA

²² Fermi National Accelerator Laboratory, MS209, P.O. Box 500, Batavia, IL 60510, USA

²³ Department of Astronomy and Astrophysics, University of Chicago, 5640 South Ellis Avenue, Chicago, IL 60637, USA

²⁴ East Asian Observatory, 660 N. A'ohoku Place, Hilo, HI 96720, USA

²⁵ James Clerk Maxwell Telescope (JCMT), 660 N. A'ohoku Place, Hilo, HI 96720, USA

²⁶ California Institute of Technology, 1200 East California Boulevard, Pasadena, CA 91125, USA

²⁷ Institute of Astronomy and Astrophysics, Academia Sinica, 645 N. A'ohoku Place, Hilo, HI 96720, USA

²⁸ Department of Physics and Astronomy, University of Hawaii at Manoa, 2505 Correa Road, Honolulu, HI 96822, USA

²⁹ Department of Physics, McGill University, 3600 rue University, Montréal, QC H3A 2T8, Canada

³⁰ Trottier Space Institute at McGill, 3550 rue University, Montréal, QC H3A 2A7, Canada

³¹ Institut de Radioastronomie Millimétrique (IRAM), 300 rue de la Piscine, F-38406 Saint Martin d'Hères, France

³² Department of Astronomy, University of Massachusetts, Amherst, MA 01003, USA

³³ Korea Astronomy and Space Science Institute, Daedeok-daero 776, Yuseong-gu, Daejeon 34055, Republic of Korea

³⁴ University of Science and Technology, Gajeong-ro 217, Yuseong-gu, Daejeon 34113, Republic of Korea

³⁵ Kavli Institute for Cosmological Physics, University of Chicago, 5640 South Ellis Avenue, Chicago, IL 60637, USA

³⁶ Department of Physics, University of Chicago, 5720 South Ellis Avenue, Chicago, IL 60637, USA

³⁷ Enrico Fermi Institute, University of Chicago, 5640 South Ellis Avenue, Chicago, IL 60637, USA

³⁸ Data Science Institute, University of Arizona, 1230 N. Cherry Ave., Tucson, AZ 85721, USA

³⁹ Program in Applied Mathematics, University of Arizona, 617 N. Santa Rita, Tucson, AZ 85721, USA

⁴⁰ Cornell Center for Astrophysics and Planetary Science, Cornell University, Ithaca, NY 14853, USA

⁴¹ Shanghai Astronomical Observatory, Chinese Academy of Sciences, 80 Nandan Road, Shanghai 200030, People's Republic of China

⁴² Key Laboratory of Radio Astronomy, Chinese Academy of Sciences, Nanjing 210008, People's Republic of China

⁴³ Physics Department, Fairfield University, 1073 North Benson Road, Fairfield, CT 06824, USA

⁴⁴ Department of Astronomy, University of Illinois at Urbana-Champaign, 1002 West Green Street, Urbana, IL 61801, USA

⁴⁵ Instituto de Astronomía, Universidad Nacional Autónoma de México (UNAM), Apdo Postal 70-264, Ciudad de México, México

⁴⁶ Institut für Theoretische Physik, Goethe-Universität Frankfurt, Max-von-Laue-Straße 1, D-60438 Frankfurt am Main, Germany

⁴⁷ Research Center for Intelligent Computing Platforms, Zhejiang Laboratory, Hangzhou 311100, People's Republic of China

⁴⁸ Tsung-Dao Lee Institute, Shanghai Jiao Tong University, Shengrong Road 520, Shanghai, 201210, People's Republic of China

⁴⁹ Department of Astronomy and Columbia Astrophysics Laboratory, Columbia University, 500 W. 120th Street, New York, NY 10027, USA

⁵⁰ Center for Computational Astrophysics, Flatiron Institute, 162 Fifth Avenue, New York, NY 10010, USA

⁵¹ Dipartimento di Fisica "E. Pancini", Università di Napoli "Federico II", Compl. Univ. di Monte S. Angelo, Edificio G, Via Cinthia, I-80126, Napoli, Italy

⁵² INFN Sez. di Napoli, Compl. Univ. di Monte S. Angelo, Edificio G, Via Cinthia, I-80126, Napoli, Italy

⁵³ Wits Centre for Astrophysics, University of the Witwatersrand, 1 Jan Smuts Avenue, Braamfontein, Johannesburg 2050, South Africa

⁵⁴ Department of Physics, University of Pretoria, Hatfield, Pretoria 0028, South Africa

⁵⁵ Centre for Radio Astronomy Techniques and Technologies, Department of Physics and Electronics, Rhodes University, Makhanda 6140, South Africa

⁵⁶ ASTRON, Oude Hoogeveensedijk 4, 7991 PD Dwingeloo, The Netherlands

⁵⁷ LESIA, Observatoire de Paris, Université PSL, CNRS, Sorbonne Université, Université de Paris, 5 place Jules Janssen, F-92195 Meudon, France

⁵⁸ JILA and Department of Astrophysical and Planetary Sciences, University of Colorado, Boulder, CO 80309, USA

⁵⁹ National Astronomical Observatories, Chinese Academy of Sciences, 20A Datun Road, Chaoyang District, Beijing 100101, People's Republic of China

⁶⁰ Las Cumbres Observatory, 6740 Cortona Drive, Suite 102, Goleta, CA 93117-5575, USA

⁶¹ Department of Physics, University of California, Santa Barbara, CA 93106-9530, USA

⁶² National Radio Astronomy Observatory, 520 Edgemont Road, Charlottesville, VA 22903, USA

⁶³ Department of Electrical Engineering and Computer Science, Massachusetts Institute of Technology, 32-D476, 77 Massachusetts Ave., Cambridge, MA 02142, USA

⁶⁴ Google Research, 355 Main St., Cambridge, MA 02142, USA

⁶⁵ Institut für Theoretische Physik und Astrophysik, Universität Würzburg, Emil-Fischer-Str. 31, D-97074 Würzburg, Germany

⁶⁶ Department of History of Science, Harvard University, Cambridge, MA 02138, USA

⁶⁷ Department of Physics, Harvard University, Cambridge, MA 02138, USA

⁶⁸ NCSA, University of Illinois, 1205 W. Clark St., Urbana, IL 61801, USA

⁶⁹ Instituto de Astronomia, Geofísica e Ciências Atmosféricas, Universidade de São Paulo, R. do Matão, 1226, São Paulo, SP 05508-090, Brazil

⁷⁰ Dipartimento di Fisica, Università degli Studi di Cagliari, SP Monserrato-Sestu km 0.7, I-09042 Monserrato (CA), Italy

⁷¹ INAF—Osservatorio Astronomico di Cagliari, via della Scienza 5, I-09047 Selargius (CA), Italy

- ⁷² INFN, sezione di Cagliari, I-09042 Monserrato (CA), Italy
- ⁷³ CP3-Origins, University of Southern Denmark, Campusvej 55, DK-5230 Odense M, Denmark
- ⁷⁴ Instituto Nacional de Astrofísica, Óptica y Electrónica. Apartado Postal 51 y 216, 72000. Puebla Pue., México
- ⁷⁵ Consejo Nacional de Ciencia y Tecnología, Av. Insurgentes Sur 1582, 03940, Ciudad de México, México
- ⁷⁶ Key Laboratory for Research in Galaxies and Cosmology, Chinese Academy of Sciences, Shanghai 200030, People's Republic of China
- ⁷⁷ Mizusawa VLBI Observatory, National Astronomical Observatory of Japan, 2-12 Hoshigaoka, Mizusawa, Oshu, Iwate 023-0861, Japan
- ⁷⁸ Department of Astronomical Science, The Graduate University for Advanced Studies (SOKENDAI), 2-21-1 Osawa, Mitaka, Tokyo 181-8588, Japan
- ⁷⁹ NOVA Sub-mm Instrumentation Group, Kapteyn Astronomical Institute, University of Groningen, Landleven 12, 9747 AD Groningen, The Netherlands
- ⁸⁰ Department of Astronomy, School of Physics, Peking University, Beijing 100871, People's Republic of China
- ⁸¹ Kavli Institute for Astronomy and Astrophysics, Peking University, Beijing 100871, People's Republic of China
- ⁸² Department of Astronomy, Graduate School of Science, The University of Tokyo, 7-3-1 Hongo, Bunkyo-ku, Tokyo 113-0033, Japan
- ⁸³ The Institute of Statistical Mathematics, 10-3 Midori-cho, Tachikawa, Tokyo, 190-8562, Japan
- ⁸⁴ Department of Statistical Science, The Graduate University for Advanced Studies (SOKENDAI), 10-3 Midori-cho, Tachikawa, Tokyo 190-8562, Japan
- ⁸⁵ Kavli Institute for the Physics and Mathematics of the Universe, The University of Tokyo, 5-1-5 Kashiwanoha, Kashiwa, 277-8583, Japan
- ⁸⁶ Leiden Observatory, Leiden University, Postbus 2300, 9513 RA Leiden, The Netherlands
- ⁸⁷ ASTRAVEO LLC, PO Box 1668, Gloucester, MA 01931, USA
- ⁸⁸ Applied Materials Inc., 35 Dory Road, Gloucester, MA 01930, USA
- ⁸⁹ Institute for Astrophysical Research, Boston University, 725 Commonwealth Ave., Boston, MA 02215, USA
- ⁹⁰ Institute for Cosmic Ray Research, The University of Tokyo, 5-1-5 Kashiwanoha, Kashiwa, Chiba 277-8582, Japan
- ⁹¹ Joint Institute for VLBI ERIC (JIVE), Oude Hoogeveensedijk 4, 7991 PD Dwingeloo, The Netherlands
- ⁹² Department of Astronomy and Atmospheric Sciences, Kyungpook National University, Daegu 702-701, Republic of Korea
- ⁹³ Kogakuin University of Technology & Engineering, Academic Support Center, 2665-1 Nakano, Hachioji, Tokyo 192-0015, Japan
- ⁹⁴ Graduate School of Science and Technology, Niigata University, 8050 Ikarashi 2-no-cho, Nishi-ku, Niigata 950-2181, Japan
- ⁹⁵ Physics Department, National Sun Yat-Sen University, No. 70, Lien-Hai Road, Kaosiung City 80424, Taiwan, R.O.C.
- ⁹⁶ National Optical Astronomy Observatory, 950 N. Cherry Ave., Tucson, AZ 85719, USA
- ⁹⁷ Department of Physics, The Chinese University of Hong Kong, Shatin, N.T., Hong Kong
- ⁹⁸ School of Astronomy and Space Science, Nanjing University, Nanjing 210023, People's Republic of China
- ⁹⁹ Key Laboratory of Modern Astronomy and Astrophysics, Nanjing University, Nanjing 210023, People's Republic of China
- ¹⁰⁰ INAF-Istituto di Radioastronomia, Via P. Gobetti 101, I-40129 Bologna, Italy
- ¹⁰¹ INAF-Istituto di Radioastronomia & Italian ALMA Regional Centre, Via P. Gobetti 101, I-40129 Bologna, Italy
- ¹⁰² Department of Physics, National Taiwan University, No. 1, Sec. 4, Roosevelt Rd., Taipei 10617, Taiwan, R.O.C
- ¹⁰³ Instituto de Radioastronomía y Astrofísica, Universidad Nacional Autónoma de México, Morelia 58089, México
- ¹⁰⁴ Yunnan Observatories, Chinese Academy of Sciences, 650011 Kunming, Yunnan Province, People's Republic of China
- ¹⁰⁵ Center for Astronomical Mega-Science, Chinese Academy of Sciences, 20A Datun Road, Chaoyang District, Beijing, 100012, People's Republic of China
- ¹⁰⁶ Key Laboratory for the Structure and Evolution of Celestial Objects, Chinese Academy of Sciences, 650011 Kunming, People's Republic of China
- ¹⁰⁷ Anton Pannekoek Institute for Astronomy, University of Amsterdam, Science Park 904, 1098 XH, Amsterdam, The Netherlands
- ¹⁰⁸ Gravitation and Astroparticle Physics Amsterdam (GRAPPA) Institute, University of Amsterdam, Science Park 904, 1098 XH Amsterdam, The Netherlands
- ¹⁰⁹ Department of Astrophysical Sciences, Peyton Hall, Princeton University, Princeton, NJ 08544, USA
- ¹¹⁰ Science Support Office, Directorate of Science, European Space Research and Technology Centre (ESA/ESTEC), Keplerlaan 1, 2201 AZ Noordwijk, The Netherlands
- ¹¹¹ School of Physics and Astronomy, Shanghai Jiao Tong University, 800 Dongchuan Road, Shanghai, 200240, People's Republic of China
- ¹¹² Institut de Radioastronomie Millimétrique (IRAM), Avenida Divina Pastora 7, Local 20, E-18012, Granada, Spain
- ¹¹³ Astronomy Department, Universidad de Concepción, Casilla 160-C, Concepción, Chile
- ¹¹⁴ National Institute of Technology, Hachinohe College, 16-1 Uwanotai, Tamonoki, Hachinohe City, Aomori 039-1192, Japan
- ¹¹⁵ Research Center for Astronomy, Academy of Athens, Soranou Efessiou 4, 115 27 Athens, Greece
- ¹¹⁶ Department of Physics, Villanova University, 800 Lancaster Avenue, Villanova, PA 19085, USA
- ¹¹⁷ Physics Department, Washington University, CB 1105, St. Louis, MO 63130, USA
- ¹¹⁸ Sejong University, 209 Neungdong-ro, Gwangjin-gu, Seoul, Republic of Korea
- ¹¹⁹ School of Physics, Georgia Institute of Technology, 837 State St NW, Atlanta, GA 30332, USA
- ¹²⁰ Department of Astronomy and Space Science, Kyung Hee University, 1732, Deogyong-daero, Giheung-gu, Yongin-si, Gyeonggi-do 17104, Republic of Korea
- ¹²¹ Canadian Institute for Theoretical Astrophysics, University of Toronto, 60 St. George Street, Toronto, ON M5S 3H8, Canada
- ¹²² Dunlap Institute for Astronomy and Astrophysics, University of Toronto, 50 St. George Street, Toronto, ON M5S 3H4, Canada
- ¹²³ Canadian Institute for Advanced Research, 180 Dundas St W, Toronto, ON M5G 1Z8, Canada
- ¹²⁴ Radio Astronomy Laboratory, University of California, Berkeley, CA 94720, USA
- ¹²⁵ Institute of Astrophysics, Foundation for Research and Technology—Hellas, Voutes, 7110 Heraklion, Greece
- ¹²⁶ Department of Physics, National Taiwan Normal University, No. 88, Sec. 4, Tingzhou Rd., Taipei 116, Taiwan, R.O.C.
- ¹²⁷ Center of Astronomy and Gravitation, National Taiwan Normal University, No. 88, Sec. 4, Tingzhou Road, Taipei 116, Taiwan, R.O.C.
- ¹²⁸ Finnish Centre for Astronomy with ESO, FI-20014 University of Turku, Finland
- ¹²⁹ Aalto University Metsähovi Radio Observatory, Metsähovintie 114, FI-02540 Kylmälä, Finland
- ¹³⁰ Gemini Observatory/NSF NOIRLab, 670 N. A'ohōkū Place, Hilo, HI 96720, USA
- ¹³¹ Frankfurt Institute for Advanced Studies, Ruth-Moufang-Strasse 1, D-60438 Frankfurt, Germany
- ¹³² School of Mathematics, Trinity College, Dublin 2, Ireland
- ¹³³ Department of Physics, University of Toronto, 60 St. George Street, Toronto, ON M5S 1A7, Canada
- ¹³⁴ Department of Physics, Tokyo Institute of Technology, 2-12-1 Ookayama, Meguro-ku, Tokyo 152-8551, Japan
- ¹³⁵ Hiroshima Astrophysical Science Center, Hiroshima University, 1-3-1 Kagamiyama, Higashi-Hiroshima, Hiroshima 739-8526, Japan
- ¹³⁶ Aalto University Department of Electronics and Nanoengineering, PL 15500, FI-00076 Aalto, Finland
- ¹³⁷ Department of Astronomy, Yonsei University, Yonsei-ro 50, Sodaemun-gu, 03722 Seoul, Republic of Korea
- ¹³⁸ National Biomedical Imaging Center, Peking University, Beijing 100871, People's Republic of China
- ¹³⁹ College of Future Technology, Peking University, Beijing 100871, People's Republic of China
- ¹⁴⁰ Department of Physics and Astronomy, University of Lethbridge, Lethbridge, AB T1K 3M4, Canada
- ¹⁴¹ Netherlands Organisation for Scientific Research (NWO), Postbus 93138, 2509 AC Den Haag, The Netherlands
- ¹⁴² Department of Physics and Astronomy, Seoul National University, Gwanak-gu, Seoul 08826, Republic of Korea
- ¹⁴³ University of New Mexico, Department of Physics and Astronomy, Albuquerque, NM 87131, USA
- ¹⁴⁴ Jeremiah Horrocks Institute, University of Central Lancashire, Preston PR1 2HE, UK
- ¹⁴⁵ Physics Department, Brandeis University, 415 South Street, Waltham, MA 02453, USA
- ¹⁴⁶ Tuorla Observatory, Department of Physics and Astronomy, University of Turku, Finland

¹⁴⁷ Radboud Excellence Fellow of Radboud University, Nijmegen, The Netherlands¹⁴⁸ School of Natural Sciences, Institute for Advanced Study, 1 Einstein Drive, Princeton, NJ 08540, USA¹⁴⁹ Princeton Gravity Initiative, Jadwin Hall, Princeton University, Princeton, NJ 08544, USA¹⁵⁰ School of Physics, Huazhong University of Science and Technology, Wuhan, Hubei, 430074, People's Republic of China¹⁵¹ Mullard Space Science Laboratory, University College London, Holmbury St. Mary, Dorking, Surrey, RH5 6NT, UK¹⁵² School of Astronomy and Space Sciences, University of Chinese Academy of Sciences, No. 19A Yuquan Road, Beijing 100049, People's Republic of China¹⁵³ Astronomy Department, University of Science and Technology of China, Hefei 230026, People's Republic of China¹⁵⁴ Department of Physics and Astronomy, Michigan State University, 567 Wilson Rd., East Lansing, MI 48824, USA

Received 2023 June 20; revised 2023 September 27; accepted 2023 October 3; published 2023 November 8

Abstract

The Event Horizon Telescope (EHT) is a millimeter very long baseline interferometry (VLBI) array that has imaged the apparent shadows of the supermassive black holes M87* and Sagittarius A*. Polarimetric data from these observations contain a wealth of information on the black hole and accretion flow properties. In this work, we develop polarimetric geometric modeling methods for mm-VLBI data, focusing on approaches that fit data products with differing degrees of invariance to broad classes of calibration errors. We establish a fitting procedure using a polarimetric “m-ring” model to approximate the image structure near a black hole. By fitting this model to synthetic EHT data from general relativistic magnetohydrodynamic models, we show that the linear and circular polarization structure can be successfully approximated with relatively few model parameters. We then fit this model to EHT observations of M87* taken in 2017. In total intensity and linear polarization, the m-ring fits are consistent with previous results from imaging methods. In circular polarization, the m-ring fits indicate the presence of event-horizon-scale circular polarization structure, with a persistent dipolar asymmetry and orientation across several days. The same structure was recovered independently of observing band, used data products, and model assumptions. Despite this broad agreement, imaging methods do not produce similarly consistent results. Our circular polarization results, which imposed additional assumptions on the source structure, should thus be interpreted with some caution. Polarimetric geometric modeling provides a useful and powerful method to constrain the properties of horizon-scale polarized emission, particularly for sparse arrays like the EHT.

Unified Astronomy Thesaurus concepts: Active galactic nuclei (16); Supermassive black holes (1663); Black hole physics (159); High angular resolution (2167); Very long baseline interferometry (1769); Polarimetry (1278)

1. Introduction

The Event Horizon Telescope (EHT) has imaged M87*, the $6.5 \times 10^9 M_{\odot}$ supermassive black hole in the M87 galaxy, in both total intensity (Event Horizon Telescope Collaboration et al. 2019a, 2019b, 2019c, 2019d, 2019e, 2019f) and linear polarization (Event Horizon Telescope Collaboration et al. 2021b, 2021a) using data from its 2017 campaign. More recently, images have been produced in circular polarization; however, these show inconsistent structure among different imaging and calibration methods owing to the weakness of the circular polarization signal, although some secure inferences on the structure could be made (Event Horizon Telescope Collaboration et al. 2023, hereafter Paper IX). The presence of resolved circular polarization structure on event horizon scales was established unambiguously, and a $\sim 4\%$ upper limit on the image-averaged resolved circular polarization fraction was obtained. While imaging methods showed different circular polarization structure between, e.g., observing epochs and frequency bands, circular polarization geometric model fitting indicated a consistent dipolar asymmetry across the multiday observing window.

In this paper, we describe and test the polarimetric modeling methods used to obtain this circular polarization modeling result. Since our modeling methods solve for the total intensity and linear polarization structure as well, we also compare our

fits to previously obtained results from EHT imaging and other geometric modeling methods. Before introducing the modeling methods, we will next briefly summarize the origin, utility, and previous measurements of linear polarization and circular polarization and the challenges of studying these quantities using very long baseline interferometry (VLBI).

1.1. Linear Polarization on Event Horizon Scales

In radiatively inefficient accretion flows onto supermassive black holes, (sub)millimeter emission is produced near the event horizon as synchrotron radiation, which is intrinsically linearly polarized at a level of $\sim 70\%$ (see, e.g., Yuan & Narayan 2014). The electric vector polarization angle (EVPA) is orthogonal to the orientation of the magnetic field. Polarimetric imaging and modeling of this emission thus probe the magnetic field structure.

However, on the photon trajectory toward the observer, the linear polarization fraction and EVPA may be altered by two effects. First, photon propagation along curved geodesics near the event horizon affects the EVPA and may lead to depolarization in the observed image (e.g., Connors & Stark 1977; Mościbrodzka et al. 2017; Narayan et al. 2021; Ricarte et al. 2022a; Palumbo & Wong 2022). Second, propagation through the magnetized accretion flow plasma results in Faraday rotation of the EVPA, with depolarizing effects as well (e.g., Mościbrodzka et al. 2017; Jiménez-Rosales & Dexter 2018; Ricarte et al. 2020). A polarized image of the accretion flow hence probes the spacetime and the plasma properties. These effects may be difficult to untangle, although Palumbo et al. (2020) found that the black hole spin can be constrained from the twistiness of the polarization pattern.

¹⁵⁵ NASA Hubble Fellowship Program, Einstein Fellow.



Original content from this work may be used under the terms of the [Creative Commons Attribution 4.0 licence](https://creativecommons.org/licenses/by/4.0/). Any further distribution of this work must maintain attribution to the author(s) and the title of the work, journal citation and DOI.

Ray-traced general relativistic magnetohydrodynamic (GRMHD) simulations show that the appearance of the horizon-scale accretion flow may indeed depend strongly on black hole and accretion parameters. In particular, magnetically arrested disk (MAD; Narayan et al. 2003) models, with large magnetic flux permeating the event horizon, produce significantly more ordered EVPA patterns than standard and normal evolution (SANE) models, due to the much larger Faraday depth and hence EVPA rotation and Faraday depolarization of the latter (e.g., Event Horizon Telescope Collaboration et al. 2021b). In addition, a lower electron temperature results in a more disordered EVPA pattern in these simulations for both SANE and MAD, again due to a larger Faraday depth. Palumbo et al. (2020) found that, despite the plasma effects, the twistiness of the EVPA pattern (the $\beta_{p,2}$ -mode; see also Section 2.3) is a proxy for black hole spin in GRMHD simulations, with larger black hole spins often resulting in more radial EVPA patterns. Ricarte et al. (2022b) showed that the handedness of the EVPA pattern switches sign as a function of radius for retrograde accretion flows, which have a black hole spin direction opposite from the large-scale plasma rotation direction.

While the total intensity EHT data of M87* from 2017 ruled out a few models from the EHT GRMHD simulation library, the linear polarization data of M87* provided stronger constraints, ruling out a significant fraction of the models in the library. These constraints favored MAD models over SANE models (Event Horizon Telescope Collaboration et al. 2021b, 2021a). In particular, the constraint on $\beta_{p,2}$ was a strong discriminator for these results. In general, our theoretical models are increasingly challenged by EHT observations, even more so for Sgr A* (Event Horizon Telescope Collaboration et al. 2022a, 2022e), where no single GRMHD library model was able to fit all constraints on the (Stokes \mathcal{I}) source structure and light curve variability (Event Horizon Telescope Collaboration et al. 2022e; Wielgus et al. 2022). Additional physics or parameter space may need to be explored.

1.2. Circular Polarization on Event Horizon Scales

Circular polarization in millimeter emission from black hole accretion flows may arise from two distinct physical processes (e.g., Wardle & Homan 2003; Mościbrodzka et al. 2021; Ricarte et al. 2021). First, synchrotron radiation is intrinsically polarized depending on the observing frequency and magnetic field strength and configuration. The maximum intrinsic circular polarization from synchrotron radiation is of order $1/\gamma$, where γ is the Lorentz factor of the (relativistic) synchrotron emitting electrons (e.g., Wardle et al. 1998; Wardle & Homan 2003). In numerical simulations of supermassive black hole accretion flows, the intrinsic circular polarization fraction comes down to $\sim 1\%$, which is substantially lower than the intrinsic linear polarization fraction of $\sim 70\%$ (Ricarte et al. 2021). Circular polarization is therefore more difficult to detect than linear polarization. The sign of intrinsic circular polarization (before any propagation effects occur) directly maps to the magnetic field orientation with respect to the emission direction, with a positive sign of the observed circular polarization corresponding to a magnetic field orientation pointing toward the observer.

Second, circular polarization may be produced from linear polarization through Faraday conversion. In the local plasma frame, Faraday conversion only operates on Stokes \mathcal{U} , while

linear polarization in synchrotron emission is intrinsically produced only in Stokes \mathcal{Q} (perpendicular to both the magnetic field and the photon propagation direction). Along the photon propagation path, part of the Stokes \mathcal{Q} thus has to be recast into Stokes \mathcal{U} for Faraday conversion to occur. Such an exchange between Stokes \mathcal{Q} and \mathcal{U} occurs in the case of Faraday rotation, where the linear polarization direction rotates depending on electron density and magnetic field component parallel to the photon propagation direction. Another pathway for Faraday conversion is a rotation of the magnetic field component perpendicular to the photon propagation direction due to a twist in the magnetic field along the photon propagation direction. Faraday conversion through Faraday rotation produces circular polarization in the same direction as the intrinsic emission (assuming a constant magnetic field). Faraday conversion through a positive twist of the magnetic field (counterclockwise with respect to the photon propagation direction) produces negative circular polarization (see, e.g., Ricarte et al. 2021, and references therein).

In general, the fraction and direction of circular polarization depend on the magnetic field structure, the electron temperature and density, and plasma composition (Jones & O’Dell 1977; Kennett & Melrose 1998; Wardle et al. 1998). These dependencies make circular polarization an excellent probe for constraining the plasma properties of black hole accretion flows.

GRMHD simulations with resolved circular polarization on sub-event-horizon scales show that the Stokes \mathcal{V} image structure strongly depends on the inclination of the viewing angle with respect to the black hole spin axis (Ricarte et al. 2021). For high inclinations (edge-on view with respect to the spin axis), the circular polarization image has a clear quadrupolar structure—especially for MAD models—set by the helical magnetic field structure of the jet in combination with the viewing angle.

For low inclinations (face-on view with respect to the spin axis), the relation between the magnetic field geometry and the Stokes \mathcal{V} image is less straightforward. The image contains contributions from features above and below the mid-plane, which have opposite sign. Stokes \mathcal{V} images from MAD models are visually dominated by the ($n = 1$) photon ring (even though its contribution to the total Stokes \mathcal{V} emission is marginal), which has an opposite sign from the direct emission due to lensing effects (photons making a half orbit around the black hole) in combination with the magnetic field geometry (Mościbrodzka et al. 2021). Stokes \mathcal{V} images from SANE models are less clearly structured, with turbulent features depending on the details of the more turbulent magnetic field and Faraday effects (Ricarte et al. 2021).

In GRMHD and semi-analytic models, the circular polarization fraction generally increases at submillimeter wavelengths as a function of positron fraction due to an increase in Faraday conversion (Anantua et al. 2020; Emami et al. 2021). However, degeneracies with other simulation parameters exist (Emami et al. 2023).

1.3. Polarimetric VLBI Data

Polarization poses particular challenges for the calibration of VLBI data. The polarization signal is often weak ($\lesssim 1\%–10\%$), especially for circular polarization. Most VLBI experiments, including the EHT, use orthogonal circular feeds, which are ideal for measuring linear polarization but require precise

calibration of the right/left (R/L) gain ratios to measure circular polarization (e.g., Homan & Wardle 1999; Homan et al. 2001; Homan & Wardle 2004; Homan & Lister 2006; Gabuzda et al. 2008, see also Section 6.2.2). Besides systematics that also affect total intensity measurements, such as rapid atmospheric phase fluctuations, atmospheric opacity, and antenna pointing offsets, polarimetric VLBI data are particularly sensitive to “leakage” effects between orthogonal feeds (see Section 3.1), which often give spurious signals that exceed the true polarized signal, especially in linear polarization. The combination of weak signals and the additional systematics has often limited polarimetric measurements, especially for circular polarization. In this work, we therefore focus on constructing data products that are invariant to most calibration errors. In this process, we can directly explore the effects of calibration errors in both the bias and uncertainty of the measurements of polarized image structure.

1.4. Outline

In this work, we provide a framework for fitting geometric models to polarimetric VLBI data, and we apply these methods to synthetic data generated from GRMHD models and to EHT observations of M87*. We introduce our polarimetric “m-ring” model in Section 2, and we outline our procedure to fit this or other geometric models to VLBI data in Section 3. We test our model fitting framework on synthetic data from geometric models in Section 4, and we apply it to synthetic data from GRMHD models in Section 5. In Section 6, we apply our methods to EHT observations of M87* in 2017, estimating the source properties in both linear and circular polarization. We conclude and provide an outlook for future work in Section 7.

2. Polarimetric m-ring Modeling

2.1. Geometric Modeling of VLBI Data

VLBI measurements, such as those made by the EHT, sample interferometric “visibilities” on each baseline connecting a pair of telescopes with mutual visibility of a target source. These visibilities are given by the correlation of the narrow-band complex electric fields sampled at the telescopes: $V_{12} \equiv \langle E_1 E_2^* \rangle$. Because each telescope can record two orthogonal polarization products (typically right and left circular, or orthogonal linear polarizations), each baseline can measure four correlations that can be easily mapped to the four Stokes parameters (see Section 3.1). By the van Cittert–Zernike theorem, these visibilities correspond to samples of the Fourier transform of the sky image, with the wavenumber given by the dimensionless baseline length (measured in wavelengths). For instance, the visibilities in total intensity \tilde{I} are given by (see, e.g., Thompson et al. 2017)

$$\tilde{\mathcal{I}}(\mathbf{u}) = \int d^2\mathbf{x} \mathcal{I}(\mathbf{x}) e^{-2\pi i \mathbf{u} \cdot \mathbf{x}}. \quad (1)$$

Here \mathbf{u} is the dimensionless baseline vector projected orthogonally to the line of sight, \mathbf{x} is the angular sky coordinate in radians, and \mathcal{I} is the sky brightness distribution. The brightness distribution $\mathcal{I}(\mathbf{x})$ is real, so the corresponding visibilities have a conjugation symmetry: $\tilde{\mathcal{I}}(\mathbf{u}) = \tilde{\mathcal{I}}^*(-\mathbf{u})$.

Because an interferometer only sparsely samples the Fourier domain, geometric modeling of interferometric data provides a powerful alternative to imaging (e.g., Pearson 1999; Event Horizon Telescope Collaboration et al. 2019f, 2022d). In

particular, for sources with relatively simple morphology, geometric models may be parameterized using far fewer parameters than imaging. Geometric models are also flexible; multiple geometric models can be easily added to describe sources with complex morphologies because the Fourier transform is linear. Geometric modeling is an especially effective analysis strategy for VLBI arrays that have a small number of baselines (such as the EHT) or in cases where the signal-to-noise ratio is low (as is frequently the case for polarimetric visibilities). The danger of using geometric models is that the choice of model may significantly affect the inferences, and model misspecification (i.e., using a model that does not fully describe the underlying structure) can result in parameter biases.

Because EHT images of M87* and Sgr A* are dominated by a prominent ring with an azimuthal brightness asymmetry (Event Horizon Telescope Collaboration et al. 2019d, 2022c), both “crescent” (Kamruddin & Dexter 2013; Benkevitch et al. 2016; Event Horizon Telescope Collaboration et al. 2019f; Wielgus et al. 2020; Lockhart & Gralla 2022) and geometric ring models (Event Horizon Telescope Collaboration et al. 2019f; Johnson et al. 2020; Event Horizon Telescope Collaboration et al. 2022c) provide good fits to EHT data from these sources.

2.2. m-ring Model

In this paper, we will focus on using extensions of the “m-ring” model from Johnson et al. (2020) to fit polarimetric EHT data. For our purposes, the principal benefits of this model are as follows:

1. Efficiency: the model has a simple analytic form in both the image and visibility domains, with analytic gradients.
2. Flexibility: the model can describe arbitrary azimuthal variations in brightness, ring shape asymmetry, and radial structure controlled by a Gaussian blurring kernel.
3. Polarimetry: the model naturally includes complex polarized structure in both linear and circular polarization.
4. Interpretability: the m-ring model naturally describes key image features that are useful for physical interpretation, such as the ring’s diameter, brightness asymmetry, shape asymmetry, and rotationally invariant polarization.

Specifically, the m-ring model is constructed from a thin ring with nonuniform brightness in azimuth expressed as a Fourier series. Written in polar image coordinates (ρ, φ) , it takes the form

$$\mathcal{I}(\rho, \varphi) = \frac{F}{\pi d} \delta\left(\rho - \frac{d}{2}\right) \sum_{k=-m}^m \beta_k e^{ik\varphi}, \quad (2)$$

where δ is the Dirac delta distribution, $\beta_{-k} \equiv \beta_k^*$ since the image is real, and $\beta_0 \equiv 1$ so that $F > 0$ gives the total flux density of the ring. By increasing the m-ring order m , increasingly complex azimuthal structures can be modeled. The corresponding visibility function in polar coordinates (u, ϕ) is given by

$$\tilde{\mathcal{I}}(u, \phi) = F \sum_{k=-m}^m \beta_k J_k(\pi d u) e^{ik(\phi - \pi/2)}, \quad (3)$$

where J_k denotes the k th Bessel function of the first kind. Notably, the azimuthal Fourier coefficients in the image and visibility domains are identical up to a constant rescaling.

Two natural extensions of this model are to include shape asymmetry and to introduce finite ring width. For the former, the m-ring can be stretched in any direction using the similarity property of the Fourier transform to compute the associated visibility function: if $\mathcal{I}(x, y) \rightarrow \mathcal{I}'(x, y) = \mathcal{I}(ax, by)$, where the arrow indicates the stretch transformation and $\mathcal{I}'(x, y)$ is the stretched m-ring, then $\tilde{\mathcal{I}}(u, v) \rightarrow \tilde{\mathcal{I}}'(u, v) = |ab|^{-1} \tilde{\mathcal{I}}(u/a, v/b)$. For the latter, the m-ring can be easily convolved with a Gaussian of FWHM α . This blurred m-ring has visibility and image functions given by

$$\mathcal{I}(\rho, \varphi; \alpha) = \frac{4 \ln 2}{\pi \alpha^2} F e^{-\frac{4 \ln 2}{\alpha^2}(\rho^2 + d^2/4)} \times \sum_{k=-m}^m \beta_k I_k \left(4 \ln 2 \frac{\rho d}{\alpha^2} \right) e^{ik\varphi}, \quad (4)$$

$$\tilde{\mathcal{I}}(u, \phi; \alpha) = \tilde{\mathcal{I}}(u, \phi) e^{-\frac{(\pi \alpha u)^2}{4 \ln 2}}, \quad (5)$$

where I_k denotes the k th modified Bessel function of the first kind.

2.3. Polarimetric m-ring Model

The m-ring model can be easily generalized to include linear and circular polarization. Each polarization product has an image determined by an associated set of Fourier coefficients; we use $\{\beta_{\mathcal{I},k}\}$ for total intensity, $\{\beta_{\mathcal{P},k}\}$ for the linear polarization,¹⁵⁶ and $\{\beta_{\mathcal{V},k}\}$ for circular polarization. Because the linear polarization is complex, there is no conjugation symmetry in the associated $\beta_{\mathcal{P},k}$. The circular polarization image is real, so $\beta_{\mathcal{V},-k} = \beta_{\mathcal{V},k}^*$. The image-integrated linear and circular polarization fractions are given by $m_{\text{net}} \equiv \beta_{\mathcal{P},0} \in \mathbb{C}$ (a complex number) and $\mathcal{V}_{\text{net}} \equiv \beta_{\mathcal{V},0} \in \mathbb{R}$ (a real number), respectively.

The only difficulty in specifying parameter ranges for the m-ring model is that it is nontrivial to enforce image positivity ($\mathcal{I}(\mathbf{x}) > 0$) and a physical polarization limit ($\mathcal{I}(\mathbf{x})^2 \geq |\mathcal{P}(\mathbf{x})|^2 + \mathcal{V}(\mathbf{x})^2$). To approximate these conditions, we typically require $|\beta_{\mathcal{I},k}| < 0.5$ (for $k \neq 0$), $|\beta_{\mathcal{P},k}| < 1$, and $|\beta_{\mathcal{V},k}| < 1$. Specifying the precise physical parameter domain is not problematic in practice because the total polarization is typically much smaller than the intensity: $\mathcal{I}(\mathbf{x})^2 \gg |\mathcal{P}(\mathbf{x})|^2 + \mathcal{V}(\mathbf{x})^2$.

Figure 1 shows examples of polarized m-rings with different parameters.

3. Polarimetric m-ring Fitting Procedure

3.1. Data Products

In VLBI observations, each antenna feed records the complex electric field E . For EHT antennas, these feeds are left and right circularly polarized,¹⁵⁷ so an antenna j records the electric fields E_{Lj} and E_{Rj} , respectively. For each pair of antennas in the array, these signals are then cross-correlated to form the cross-correlation matrix ρ_{jk} , which in the absence of any other observational effects can be written in terms of the

Stokes visibility components $\tilde{\mathcal{I}}, \tilde{\mathcal{Q}}, \tilde{\mathcal{U}}$, and $\tilde{\mathcal{V}}$ as

$$\rho_{jk} = \begin{pmatrix} \langle E_{Rj} E_{Rk}^* \rangle & \langle E_{Rj} E_{Lk}^* \rangle \\ \langle E_{Lj} E_{Rk}^* \rangle & \langle E_{Lj} E_{Lk}^* \rangle \end{pmatrix} \equiv \begin{pmatrix} R_j R_k^* & R_j L_k^* \\ L_j R_k^* & L_j L_k^* \end{pmatrix} \\ = \begin{pmatrix} \tilde{\mathcal{I}}_{jk} + \tilde{\mathcal{V}}_{jk} & \tilde{\mathcal{Q}}_{jk} + i\tilde{\mathcal{U}}_{jk} \\ \tilde{\mathcal{Q}}_{jk} - i\tilde{\mathcal{U}}_{jk} & \tilde{\mathcal{I}}_{jk} - \tilde{\mathcal{V}}_{jk} \end{pmatrix} \\ \equiv \begin{pmatrix} \tilde{\mathcal{I}}_{jk} + \tilde{\mathcal{V}}_{jk} & \tilde{\mathcal{P}}_{jk} \\ \tilde{\mathcal{P}}_{jk}^* & \tilde{\mathcal{I}}_{jk} - \tilde{\mathcal{V}}_{jk} \end{pmatrix}. \quad (6)$$

However, this relation does not hold for imperfect instruments. Observational effects affecting this relation can be categorized in the gain matrix \mathbf{G} , the leakage matrix \mathbf{D} , and the field rotation matrix Φ . For each antenna j , they are combined in the Jones matrix

$$\mathbf{J}_j = \mathbf{G}_j \mathbf{D}_j \Phi_j = \begin{pmatrix} G_{jR} & 0 \\ 0 & G_{jL} \end{pmatrix} \begin{pmatrix} 1 & D_{jR} \\ D_{jL} & 1 \end{pmatrix} \begin{pmatrix} e^{-i\phi_j} & 0 \\ 0 & e^{i\phi_j} \end{pmatrix}. \quad (7)$$

The measured correlation matrix is then given by the radio interferometer measurement equation (RIME; Hamaker et al. 1996; Smirnov 2011)

$$\rho'_{jk} = \mathbf{J}_j \rho_{jk} \mathbf{J}_k^\dagger. \quad (8)$$

The Stokes \mathcal{I} and \mathcal{V} information is primarily contained in the parallel-hand visibilities (Roberts et al. 1994):

$$R_j R_k^* = G_{jR} G_{kR}^* \left[(\tilde{\mathcal{I}}_{jk} + \tilde{\mathcal{V}}_{jk}) e^{i(\phi_k - \phi_j)} + D_{jR} D_{kR}^* (\tilde{\mathcal{I}}_{jk} - \tilde{\mathcal{V}}_{jk}) e^{i(\phi_j - \phi_k)} + D_{jR} \tilde{\mathcal{P}}_{kj}^* e^{i(\phi_j + \phi_k)} + D_{kR}^* \tilde{\mathcal{P}}_{jk} e^{i(-\phi_j - \phi_k)} \right], \\ L_j L_k^* = G_{jL} G_{kL}^* \left[(\tilde{\mathcal{I}}_{jk} - \tilde{\mathcal{V}}_{jk}) e^{i(\phi_j - \phi_k)} + D_{jL} D_{kL}^* (\tilde{\mathcal{I}}_{jk} + \tilde{\mathcal{V}}_{jk}) e^{i(\phi_k - \phi_j)} + D_{jL} \tilde{\mathcal{P}}_{jk} e^{i(-\phi_j - \phi_k)} + D_{kL}^* \tilde{\mathcal{P}}_{kj}^* e^{i(\phi_j + \phi_k)} \right]. \quad (9)$$

From these parallel-hand visibilities, we can construct two data products that are especially suitable for fitting the Stokes \mathcal{V} structure. First, we can fit to the parallel-hand visibility ratios, $R_j R_k^* / L_j L_k^*$. Assuming that the leakage terms have been well corrected and the fractional linear polarization is small, dropping the terms proportional to D^2 and $D\tilde{\mathcal{P}}$, $R_j R_k^* / L_j L_k^*$ (hereafter referred to as RR/LL) to first order depends on the fractional circular polarization in the visibility domain:

$$\frac{R_j R_k^*}{L_j L_k^*} \approx \frac{G_{jR} G_{kR}^*}{G_{jL} G_{kL}^*} e^{2i(\phi_k - \phi_j)} \frac{\tilde{\mathcal{I}}_{jk} + \tilde{\mathcal{V}}_{jk}}{\tilde{\mathcal{I}}_{jk} - \tilde{\mathcal{V}}_{jk}} \\ = \frac{G_{jR} G_{kR}^*}{G_{jL} G_{kL}^*} e^{2i(\phi_k - \phi_j)} \left(1 + 2 \frac{\tilde{\mathcal{V}}_{jk}}{\tilde{\mathcal{I}}_{jk}} + \mathcal{O} \left(\frac{\tilde{\mathcal{V}}_{jk}^2}{\tilde{\mathcal{I}}_{jk}^2} \right) \right). \quad (10)$$

This data product has the advantage of canceling rapid atmospheric phase variations, since the atmosphere is not significantly birefringent at millimeter wavelengths (i.e., its refractive index is independent of polarization). However, the visibility ratios depend on the R/L gain ratios. These are often

¹⁵⁶ We generally work with the complex linear polarization field, $\mathcal{P} \equiv \mathcal{Q} + i\mathcal{U}$, rather than the individual Stokes parameters.

¹⁵⁷ An exception is ALMA, which has linear feeds. The mixed-basis correlations are converted to a circular basis with PolConvert (Martí-Vidal et al. 2016).

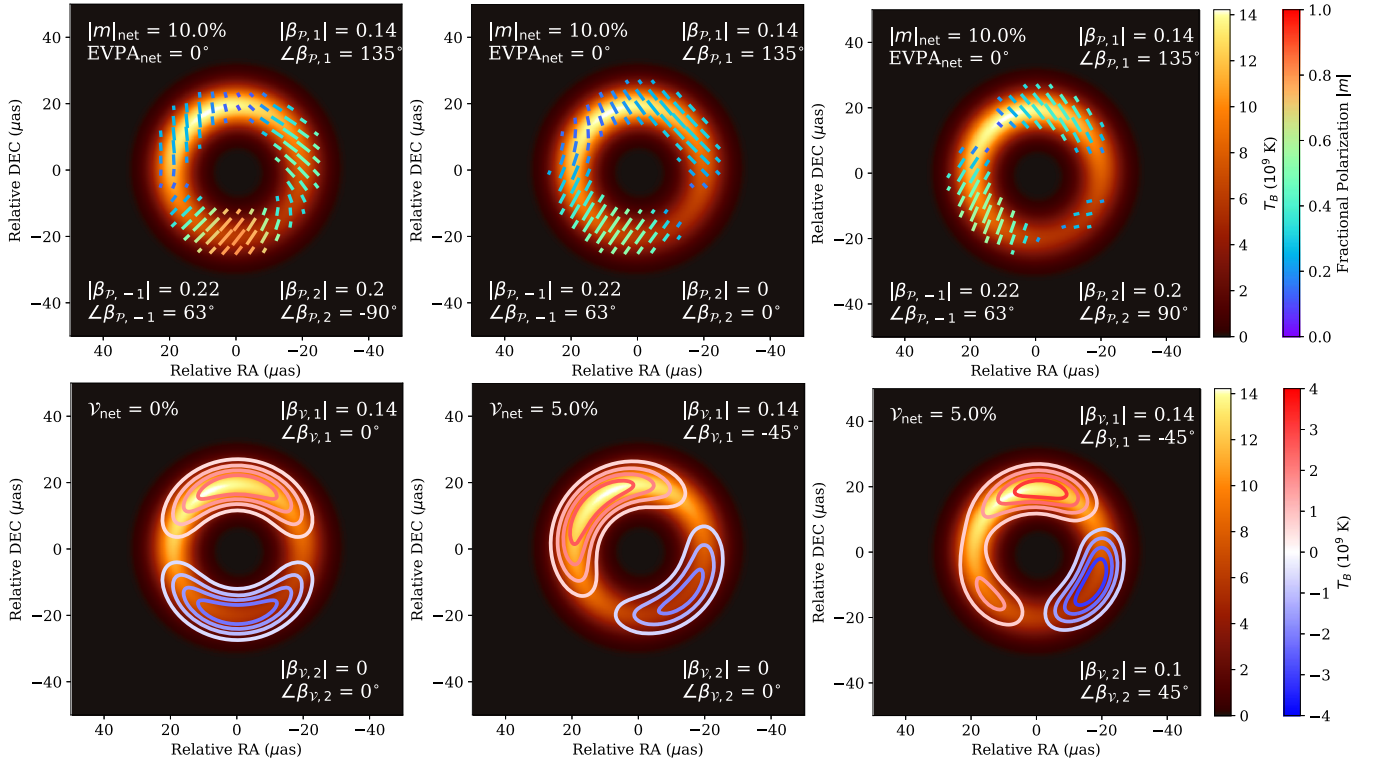


Figure 1. Examples of three m-ring models in Stokes \mathcal{I} and \mathcal{P} (top panels) and Stokes \mathcal{I} and \mathcal{V} (bottom panels). Throughout the panels, the Stokes \mathcal{I} structure (heat map) is kept constant with $F = 0.5$ Jy, $d = 40$ μs , $\alpha = 10$ μs , and $\beta_{\mathcal{T},1} = 0.2\text{--}0.1i$. The top middle panel shows a linear polarization structure with $m_{\text{net}} \equiv \beta_{\mathcal{P},0} = 0.1$, $\beta_{\mathcal{P},-1} = 0.1 + 0.2i$, and $\beta_{\mathcal{P},1} = -0.1 + 0.1i$. In the top left and right panels, nonzero $\beta_{\mathcal{P},2}$ components have been added with opposite sign. The bottom left panel shows a dipolar circular polarization structure (contours) oriented toward the north ($\beta_{\mathcal{V},1} = 0.14$). The net circular polarization is zero, so that the north and south half of the ring are identical with opposite sign in Stokes $\beta_{\mathcal{V}}$. In the bottom middle panel, we have rotated the circular polarization structure by -45° and introduced a nonzero net circular polarization ($\gamma_{\text{net}} \equiv \beta_{\mathcal{V},0} = 0.05$), so that the symmetry is broken. Finally, in the bottom right panel we have added a nonzero $\beta_{\mathcal{V},2}$ component, increasing the complexity of the azimuthal structure in Stokes \mathcal{V} . The model shown in the middle panels is used for our geometric tests (Section 4, Figure 3).

stable over many hours and can be corrected, although some EHT sites have shown rapidly variable R/L gain ratios (Paper IX; see also Section 6.2.2). Since the gain ratios are antenna based and multiplicative while the circular polarization signal is baseline based and additive, complex circular polarization structure may be extracted from the RR/LL data product even if the R/L gain ratio calibration is imperfect (see also Homan & Wardle 1999).

Alternatively, we can fit to the parallel-hand closure phases and closure amplitudes. Closure phase is the sum of visibility phases on a triangle of baselines, and closure amplitudes are ratios of visibility products on a quadrangle of baselines (e.g., Thompson et al. 2017). These data products are independent of multiplicative station-based calibration errors, including the gains as they cancel in the sums and products, respectively. The closure products are not independent of other station-based calibration errors, such as polarimetric leakage and bandpass errors. For EHT data, estimated residual leakages are only $\sim 1\%$ (Event Horizon Telescope Collaboration et al. 2021a) and thus have a negligible effect unless polarization fractions are very high. Noting that $R_j R_k^* \approx \tilde{\mathcal{I}}_{jk}(1 + \tilde{\mathcal{V}}_{jk}/\tilde{\mathcal{I}}_{jk})$ and $L_j L_k^* \approx \tilde{\mathcal{I}}_{jk}(1 - \tilde{\mathcal{V}}_{jk}/\tilde{\mathcal{I}}_{jk})$, it becomes apparent that a nonconstant fractional circular polarization leads to phase and amplitude differences between the parallel hands, which can be robustly detected by investigating the gain-invariant closure products. However, closure quantities contain less information than the baseline-based visibility ratios when prior knowledge on the gains is available (e.g., Blackburn et al. 2020). In total intensity, closure phases deviating from 0° or 180° indicate the presence of non-point-symmetric structure (e.g., Monnier 2007). In circular polarization, nonzero differences between LL^* and RR^* closure phases on a given triangle and time indicate the presence of

nonconstant fractional circular polarization structure (see Figure 2 for examples).

Thus, comparing the results of fits to these two types of data products brackets the range of uncertainty in the Stokes \mathcal{V} structure, with smaller uncertainties expected for the visibility ratios (tied to our confidence in the a priori R/L gain calibration) and larger uncertainties for the closure products (with fewer calibration assumptions required).

In addition to this information in the parallel-hand visibilities, the cross-hand visibilities contain information about the linear polarization structure of the source (see, e.g., Roberts et al. 1994):

$$\begin{aligned}
 R_j L_k^* &= G_{jR} G_{kL}^* \left[\tilde{\mathcal{P}}_{jk} e^{i(-\phi_k - \phi_j)} \right. \\
 &\quad + D_{jR} D_{kL}^* \tilde{\mathcal{P}}_{kj}^* e^{i(\phi_j + \phi_k)} \\
 &\quad + D_{jR} (\tilde{\mathcal{I}}_{jk} - \tilde{\mathcal{V}}_{jk}) e^{i(-\phi_k + \phi_j)} \\
 &\quad \left. + D_{kL}^* (\tilde{\mathcal{I}}_{jk} + \tilde{\mathcal{V}}_{jk}) e^{i(-\phi_k + \phi_j)} \right], \\
 L_j R_k^* &= G_{jL} G_{kR}^* \left[\tilde{\mathcal{P}}_{kj} e^{i(\phi_k + \phi_j)} \right. \\
 &\quad + D_{jL} D_{kR}^* \tilde{\mathcal{P}}_{jk}^* e^{i(-\phi_j - \phi_k)} \\
 &\quad + D_{jL} (\tilde{\mathcal{I}}_{jk} + \tilde{\mathcal{V}}_{jk}) e^{i(-\phi_k + \phi_j)} \\
 &\quad \left. + D_{kR}^* (\tilde{\mathcal{I}}_{jk} - \tilde{\mathcal{V}}_{jk}) e^{i(\phi_k - \phi_j)} \right]. \quad (11)
 \end{aligned}$$

Since the leakage terms here enter in products $D\tilde{\mathcal{I}}$ rather than $D\tilde{\mathcal{P}}$ (Equation (9)), it is of greater importance to calibrate them for a faithful linear polarization source reconstruction.

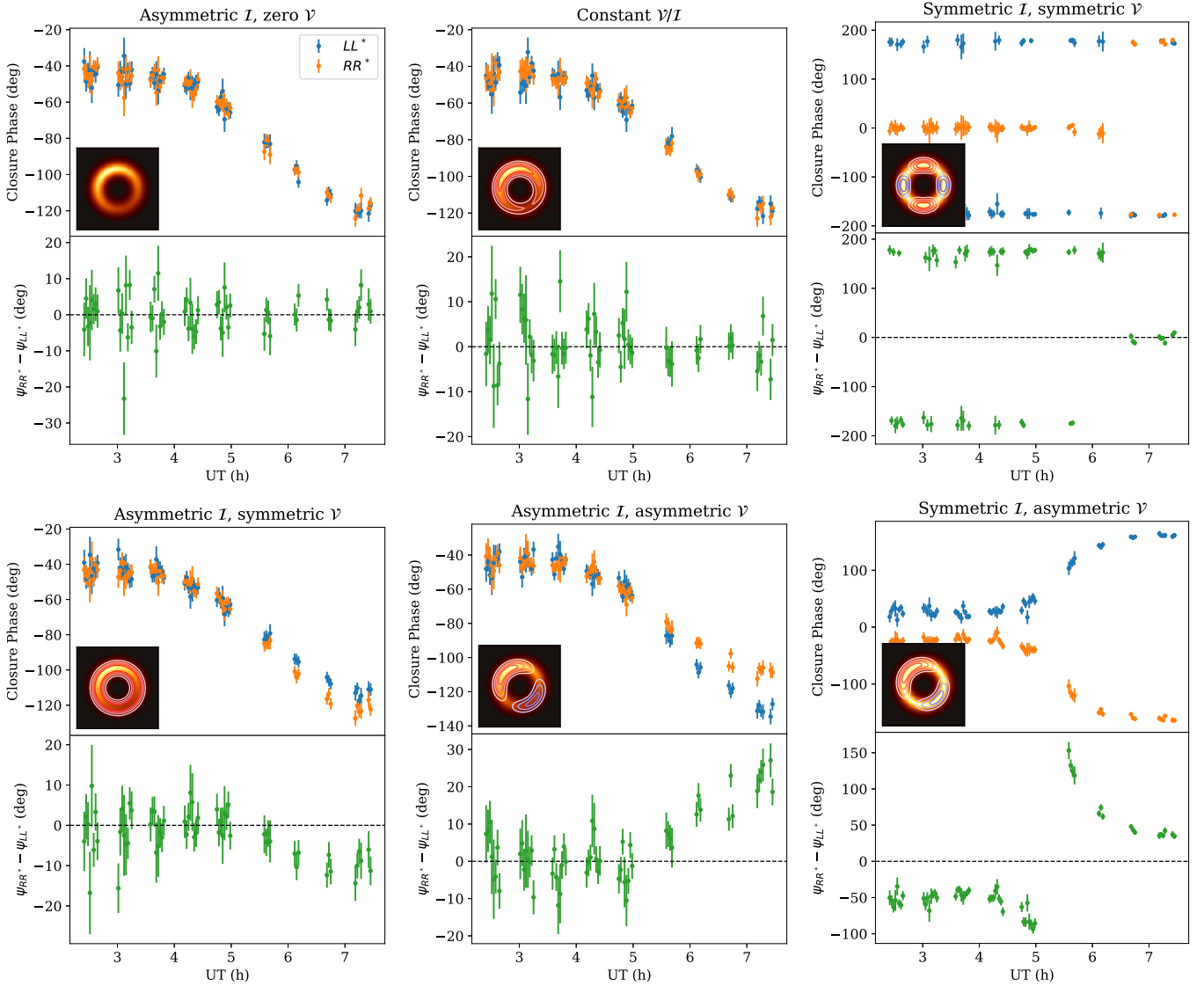


Figure 2. LL^* (blue) and RR^* (orange) closure phases and their differences (green) on the ALMA-SMT-LMT triangle for m-ring models with different combinations of point-symmetric and non-point-symmetric total intensity and circular polarization structures, simulated with 2017 April 11 EHT coverage and thermal noise. The $\beta_{\mathcal{I}}$ parameters are the same as those in Figure 1, except for the rightmost panels, where $\beta_{\mathcal{I},1} = 0$. In models with asymmetric Stokes \mathcal{V} structure, the $\beta_{\mathcal{V}}$ parameters are the same as those in the bottom middle panel of Figure 1, and for the models with symmetric Stokes \mathcal{V} structure, $\beta_{\mathcal{V},0} = 0.1$ and $\beta_{\mathcal{V},1} = 0$, with $\beta_{\mathcal{V},2} = 0.2$ in the top right panel. The bottom middle model is identical to the bottom middle model in Figure 1. A constant fractional circular polarization structure results in identical closure phases in both parallel hands (top left and middle panels). If the fractional circular polarization structure is not constant, the parallel-hand closure phase differences are nonzero (bottom and top right panels). In the top right panel, the fractional circular polarization is point-symmetric but not constant, and the closure phase differences are 0° or 180° .

Neglecting D^2 , $D\tilde{\mathcal{P}}$, and \mathcal{V} terms, we can use Equations (9) and (11) to construct the cross-hand-to-parallel-hand visibility ratios (Roberts et al. 1994; Johnson et al. 2015)

$$\begin{aligned}
 \frac{L_j R_k^*}{L_j L_k^*} &\approx \frac{G_{kR}^*}{G_{kL}^*} \left[\check{m}_{kj}^* e^{2i\phi_k} + D_{jL} e^{-2i(\phi_j - \phi_k)} + D_{kR}^* \right], \\
 \frac{L_j R_k^*}{R_j R_k^*} &\approx \frac{G_{jL}}{G_{kR}} \left[\check{m}_{kj}^* e^{2i\phi_j} + D_{jL} + D_{kR}^* e^{2i(\phi_j - \phi_k)} \right], \\
 \frac{R_j L_k^*}{L_j L_k^*} &\approx \frac{G_{jR}}{G_{jL}} \left[\check{m}_{jk} e^{2i\phi_j} + D_{jR} + D_{kL}^* e^{-2i(\phi_j - \phi_k)} \right], \\
 \frac{R_j L_k^*}{R_j R_k^*} &\approx \frac{G_{kL}^*}{G_{kR}^*} \left[\check{m}_{jk} e^{2i\phi_k} + D_{jR} e^{2i(\phi_j - \phi_k)} + D_{kL}^* \right]. \quad (12)
 \end{aligned}$$

Here $\check{m}_{jk} = \tilde{\mathcal{P}}_{jk}/\tilde{\mathcal{I}}_{jk}$ is the polarimetric ratio in the visibility domain. This quantity, while not the Fourier transform of its image domain analog $m = \mathcal{P}/\mathcal{I}$, has proven useful in capturing linear polarization source structure (Johnson et al. 2015; Gold et al. 2017). Phase fluctuations cancel in the correlation ratios, and the correlation ratios only depend on left-to-right gain ratios rather than left and right gains separately. Instrumental polarization leakage remains a source of systematic error, and it can be calibrated by observing the source and a set of calibrators across a wide range of field rotation angle.

Another calibration-invariant data product containing polarization information is the closure trace, which is formed on a quadrangle of baselines (Broderick & Pesce 2020). Closure traces are a natural extension of closure amplitudes and closure phases into full Stokes. They are insensitive to both station

gains and polarimetric leakage and hence allow for maximum calibration freedom. They may also provide an unambiguous detection of nontrivial polarization image structure, although linear and circular polarization cannot be distinguished in such a test. Since we have a decent handle on the EHT 2017 D-terms and gains, we utilize that information in our fits by fitting to \tilde{m} rather than closure traces. We use closure traces for consistency checks in Paper IX.

3.2. Fitting Implementation

Our polarimetric model fitting methods have been implemented in `eht-imaging` (Chael et al. 2016, 2018, 2019). This Python library contains many utilities for the analysis of VLBI data, including functions for common operations (e.g., data flagging, averaging, network calibration) on VLBI data sets, plotting utilities, static and dynamic imaging tools, synthetic data generation tools, an interstellar scattering module, and most recently geometric modeling (e.g., Event Horizon Telescope Collaboration et al. 2022d). Within the modeling module, several geometric models have been implemented apart from the m-ring model, including point sources, Gaussians, disks, crescents, and rings. These models can be flexibly combined to form a multicomponent source model. For our m-ring fits, we set flat priors (uniform between minimum and maximum values) for all source parameters. For posterior exploration, we use the `dynesty` sampler (Speagle 2020).

3.3. Data Preprocessing and Treatment of Zero-baseline Parameters

Before performing any fitting, we preprocess our data sets in several ways. As typically done for analysis of EHT data sets (e.g., Event Horizon Telescope Collaboration et al. 2019d, 2022b, 2022c, 2022d), we add a small fraction (estimated at around 2%; Event Horizon Telescope Collaboration et al. 2019c) of the visibility amplitudes to the thermal error budget in quadrature, effectively acting as a regularization and imposing a maximal signal-to-noise ratio in order to represent residual systematic errors. These systematic uncertainties are added to each data point; thus, they impact both visibilities and interferometric closure products. For our fits to *RR/LL* visibility ratios, this fractional noise absorbs systematic uncertainties in the *R/L* gain ratios. For our fits to closure data products, the fractional noise covers nonclosing errors. Apart from polarimetric leakage, the main source of these additional nonclosing uncertainties is related to gain calibration of wide frequency bands (e.g., Natarajan et al. 2022). We add the 2% noise to GRMHD synthetic data sets generated without nonclosing errors as well in order to maintain consistency in the data preprocessing, but the effect on the closure product noise budget is generally small. Apart from adding fractional noise, we also preprocess our data by performing scan averages. This operation increases signal-to-noise ratios and reduces the number of data points that need to be fit, making the process more efficient. Finally, we may rescale zero-baseline fluxes depending on the data set. During the generation of the synthetic GRMHD data sets (Paper IX, Section 5), a large-scale component was added to the visibilities to mimic large-scale structure seen in the EHT M87* data. For our fits to these data sets, we added a large-scale circular Gaussian (FWHM 2 mas) model component with

the same total flux and polarization parameters as this added component and kept these parameters fixed while fitting the compact structure with the polarized m-ring model. For the real EHT M87* data, we used the data sets where the large-scale structure was taken out by rescaling the zero baselines (Paper IX).

Circular polarization fitting to the parallel-hand closure products does not constrain the integrated fractional circular polarization $\mathcal{V}_{\text{net}}/\mathcal{I}_{\text{tot}}$. The zero-baseline *LL* visibilities measure $\mathcal{I}_{\text{tot}} + \mathcal{V}_{\text{net}}$, and the *RR* visibilities are sensitive to $\mathcal{I}_{\text{tot}} - \mathcal{V}_{\text{net}}$ (Equation (9)), but the closure products containing zero baselines cannot distinguish between these. During the fitting, we therefore fix \mathcal{V}_{net} to the ground-truth value for synthetic data sets and to the measured \mathcal{V}_{net} from zero-baseline observations (ALMA-only; Goddi et al. 2021) for real M87* data. For consistency, we also fix \mathcal{V}_{net} for our fits to right-to-left visibility ratios. We investigate the effect of varying \mathcal{V}_{net} on our M87* fits in Section 6.2.

4. Tests on Synthetic Data from Geometric Models

To further outline, motivate, and test our polarimetric fitting procedure, we start by fitting polarized m-rings to synthetic EHT data generated from the same model. Thus, the model specification is perfect for these tests. In particular, we use these tests on geometric models to establish a preferred fitting procedure that is free of biases, at least in these idealized cases. As shown below, biases may be introduced by not fitting the Stokes \mathcal{I} and \mathcal{V} structure simultaneously, by fitting the Stokes \mathcal{V} structure without taking the linear polarization structure and leakage effects into account, and by fitting to the *RR/LL* data product in the presence of nonunity *R/L* gain ratios. Once the fitting procedures have been established and tested, we move on to the more realistic case of GRMHD models in Section 5.

4.1. Model Description and Synthetic Data Generation

For the geometric model tests, we used a circularly polarized m-ring model with $F = 0.5$ Jy, $d = 40$ μas , $\alpha = 10$ μas , $\beta_{\mathcal{I},1} = 0.2 - 0.1i$, $\beta_{\mathcal{V},0} = 0.05$, and $\beta_{\mathcal{V},1} = 0.1 - 0.1i$. This model is shown in the middle panel of Figure 1. The net circular polarization fraction of 5% is substantially higher than observed for most VLBI sources, as is the resolved circular polarization fraction of up to $\sim 40\%$ (Section 5 shows more realistic cases). In order to test the effect of linear polarization structure and leakage, we also generated a model with added linear polarization by setting $\beta_{\mathcal{P},0} = 0.1$, $\beta_{\mathcal{P},-1} = 0.1 + 0.2i$, and $\beta_{\mathcal{P},1} = -0.1 + 0.1i$.

Synthetic data were generated with `eht-imaging` (Chael et al. 2016, 2018), using the *uv*-coverage and thermal noise from the synthetic data sets generated for the imaging and modeling method tests in Paper IX (see also Section 5.1), corresponding to the low-band EHT M87* data set from 2017 April 11. Since these tests focus on the effect of fitting procedure choices and the presence of linear polarization and leakage, we did not introduce any systematic gain offsets for these tests. Such effects are introduced in our GRMHD model fits (Section 5). For the tests with linear polarization, we set the left leakage terms $D_{jL} = 0.04 + 0.04i$ and the right leakage terms $D_{jR} = 0.03 + 0.03i$ for all stations.

4.2. Fitting Procedures and Results

Figure 3 shows $\beta_{\mathcal{V},1}$ posteriors from fits to our geometric models using different fitting procedures and data products. In general, fits to closure quantities result in wider posteriors than fits to *RR/LL* visibility ratios, which is expected given that there is more information in the latter.

The top row of Figure 3 shows the importance of fitting for the Stokes \mathcal{I} and \mathcal{V} structure simultaneously. Polarimetric reconstructions are often made by first reconstructing the Stokes \mathcal{I} structure and keeping that frozen while reconstructing the polarimetric structure (e.g., Event Horizon Telescope Collaboration et al. 2021a). Taking a similar approach here results in the blue curves in the top panels of Figure 3. Here the Stokes \mathcal{I} m-ring parameters were fixed to the posterior maximum (MAP) of the Stokes \mathcal{I} fit before fitting the Stokes \mathcal{V} structure. This strategy results in a small (a few percent) but statistically significant bias. Small errors in the Stokes \mathcal{I} parameters propagate to a biased estimate of the Stokes \mathcal{V} parameters, as the parallel-hand visibilities, which are the data products used for the fits, contain contributions from both (Equation (9)). Fitting for the Stokes \mathcal{I} and \mathcal{V} structure simultaneously (orange curves) is computationally more expensive but removes the biases.

The middle row of Figure 3 shows another potential source of biases in the Stokes \mathcal{V} posteriors. For these fits, the ground-truth source model included linear polarization structure, and polarization leakage was introduced in the synthetic data generation (Section 4). The blue curves show posteriors resulting from fitting the Stokes \mathcal{I} and \mathcal{V} structure simultaneously, but ignoring the linear polarization structure and leakage. While the fit to closure quantities is acceptable, a significant bias is present for the fit to the *RR/LL* visibility ratios. Even though the linear polarization structure and leakage enters the parallel-hand visibilities only as a second-order effect (Equation (9)), they may still cause the circular polarization fits to be biased and therefore should be included in the Stokes \mathcal{V} fitting process. The orange curves were obtained by first fitting the Stokes \mathcal{I} structure, then fitting the linear polarization structure and leakage parameters, and subsequently fixing the linear polarization structure and leakage parameters to the MAP while fitting for the Stokes \mathcal{I} and \mathcal{V} structure simultaneously. This strategy removes the biases introduced when ignoring the linear polarization structure and leakage effects.

Finally, the bottom row of Figure 3 shows that when introducing *R/L* gain amplitude offsets (here set to be constant in time), the calibration-invariant closure-only posteriors are not affected, while the *R/L* gain-sensitive *RR/LL* posteriors (Equation (9)) show increasing biases with increasing *R/L* gain offsets. In practice, it is thus important that the *R/L* gain ratios are calibrated as well as possible when fitting to *RR/LL* visibility ratios from real data sets. Since closure products are not affected by these gain offsets, checking for consistency with closure-only fits is recommended (see also Section 6).

5. Application to Synthetic Data from GRMHD Models

In this section, we apply our polarimetric m-ring fitting procedures to synthetic EHT data from a set of three GRMHD models, investigating in particular how well the basic (asymmetric) linear and circular structure can be recovered for different GRMHD parameters, and how the geometric fits behave as a function of the Stokes \mathcal{V} m-ring order $m_{\mathcal{V}}$. The

synthetic data sets were generated for the circular polarization imaging and modeling tests described in Paper IX. Here we discuss the m-ring modeling results in greater depth.

5.1. Model Description and Synthetic Data Generation

The three GRMHD models 1 (MAD, $a_* = -0.5$), 2 (MAD, $a_* = 0.5$), and 3 (SANE, $a_* = 0$) have different levels of resolved circular polarization. The image-averaged, total-intensity-weighted circular polarization fraction, $\langle |\mathcal{V}/\mathcal{I}| \rangle$, is approximately 0.5%, 2%, and 4%, respectively, for the three models. All models pass linear and total circular polarization constraints from Event Horizon Telescope Collaboration et al. (2021a) and Goddi et al. (2021).

Synthetic data were generated using `eht-imaging` for low-band EHT M87* *uv*-coverage on 2017 April 11. Thermal noise and systematic gain and leakage terms were added, and nonunity left-to-right gain ratios G_R/G_L were introduced for all sites except ALMA. The G_R/G_L amplitudes were sampled from a Gaussian distribution with unity mean and a 20% standard deviation, with a 2 hr correlation timescale. For the G_R/G_L phases, a standard deviation of 10° (40° for the SMA station) and a 24 hr correlation timescale were used. These numbers were motivated by a priori limits estimated for the 2017 EHT data (Paper IX). More details on the GRMHD models and data generation are reported in Paper IX.

To quantitatively compare our fits to the ground-truth model, we compute the ground-truth $\beta_{\mathcal{P},k}$ (and analogously the $\beta_{\mathcal{V},k}$) in the image domain (see, e.g., Palumbo et al. 2020) as

$$\beta_{\mathcal{P},k} = \frac{1}{\mathcal{I}_{\text{tot}}} \int_{\rho_{\text{min}}}^{\rho_{\text{max}}} \int_0^{2\pi} \mathcal{P}(\rho, \phi) e^{-ik\phi} \rho d\phi d\rho, \quad (13)$$

where we set the inner radius ρ_{min} to zero and the outer radius ρ_{max} to a large value (outside the field of view) in order to capture the full model image.

5.2. Linear Polarization Results

Figure 4 shows total intensity and linear polarization m-ring fits ($m_{\mathcal{I}} = 3$, $m_{\mathcal{P}} = 3$) to synthetic data from the three GRMHD models. While a comparison by eye shows many low-order features being recovered by the modeling, some systematic offsets clearly remain, which we attribute to model misspecification. The total polarization fraction is recovered least accurately for model 3, which was challenging to fit with the m-ring model owing to the extended emission outside the photon ring and the high degree of asymmetry, concentrating most total intensity and polarized emission in the South. The net EVPA is recovered within a few degrees for models 2 and 3 but not for model 1, which has small net polarization fraction and the most complex EVPA structure. $\angle\beta_{\mathcal{P},2}$ is recovered to within 12° – 34° , and $|\beta_{\mathcal{P},2}|$ to within 0.01.

Overall, model 2 is fit best, which can be attributed to a simple twisty polarization pattern centered on the photon ring, which lends itself especially well to m-ring modeling. Such a polarization pattern is seen in many MAD GRMHD models. Models 1 and 3 both show most emission outside the photon ring, due to model 1 being a model with retrograde spin and model 3 being a SANE model with zero spin (SANE and zero-spin models have been ruled out for M87*; Event Horizon Telescope Collaboration et al. 2019e, 2021b). As is made clear from these results, the ability of m-ring modeling to constrain

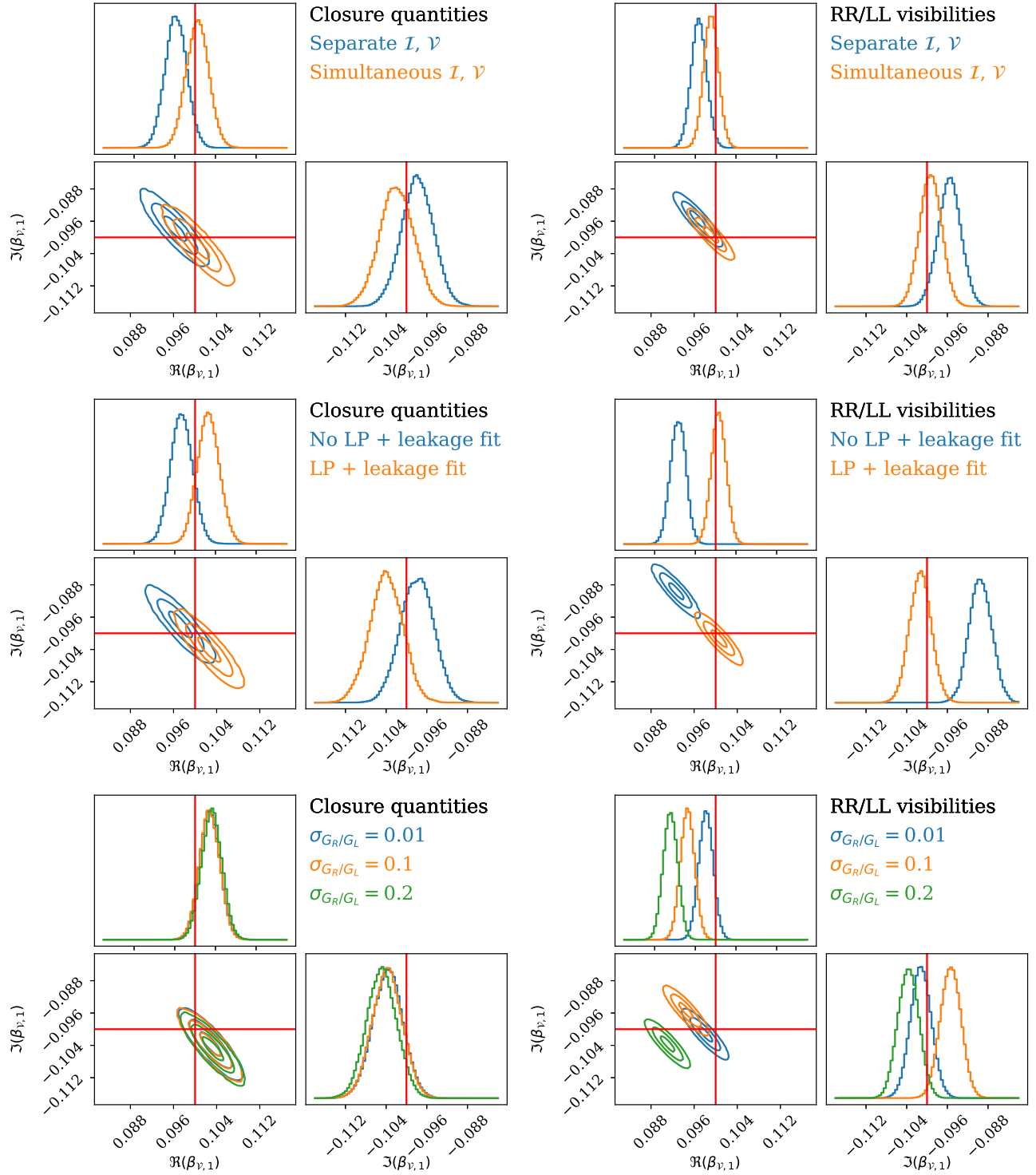


Figure 3. $\beta_{\nu,1}$ posteriors from fitting a circularly polarized m-ring to synthetic EHT 2017 data generated from two different m-ring models. Ground-truth values are indicated with red vertical and horizontal lines and correspond to the middle panel of Figure 1. Fits using closure quantities are shown on the left, and fits with *RR/LL* visibility ratios are shown on the right. The posteriors on the top row were computed from fits to data generated from a model with zero linear polarization and without any leakage corruptions added to the data. Each top row panel compares separate (consecutive) Stokes \mathcal{I} and \mathcal{V} fits (blue) vs. simultaneous Stokes \mathcal{I} and \mathcal{V} fits (orange). The posteriors in the middle row were computed from simultaneous Stokes \mathcal{I} and \mathcal{V} fits to data generated from a model with nonzero linear polarization and with leakage corruptions added to the data. Each middle row panel compares fits ignoring linear polarization and leakage fits (blue) to fits including linear polarization and leakage fits (orange). The bottom row shows comparisons between applying different *R/L* gain ratio offsets to the synthetic data before fitting. The contours show 1σ , 2σ , and 3σ levels. In general, the fits using only closure quantities have slightly weaker constraints, and both data products show biases when fitting Stokes \mathcal{V} separate from \mathcal{I} ; *RR/LL* visibility ratios show biases when ignoring the presence of linear polarization and leakage effects and when *R/L* gain offsets are present in the data.

the polarization structure depends on the similarity of the model to the ground truth, which is indeed the most important caveat for any geometric modeling result. As shown in

Section 6, it appears that M87* as observed by the EHT is well suited for linear polarization m-ring modeling, given the excellent agreement between imaging and modeling results.

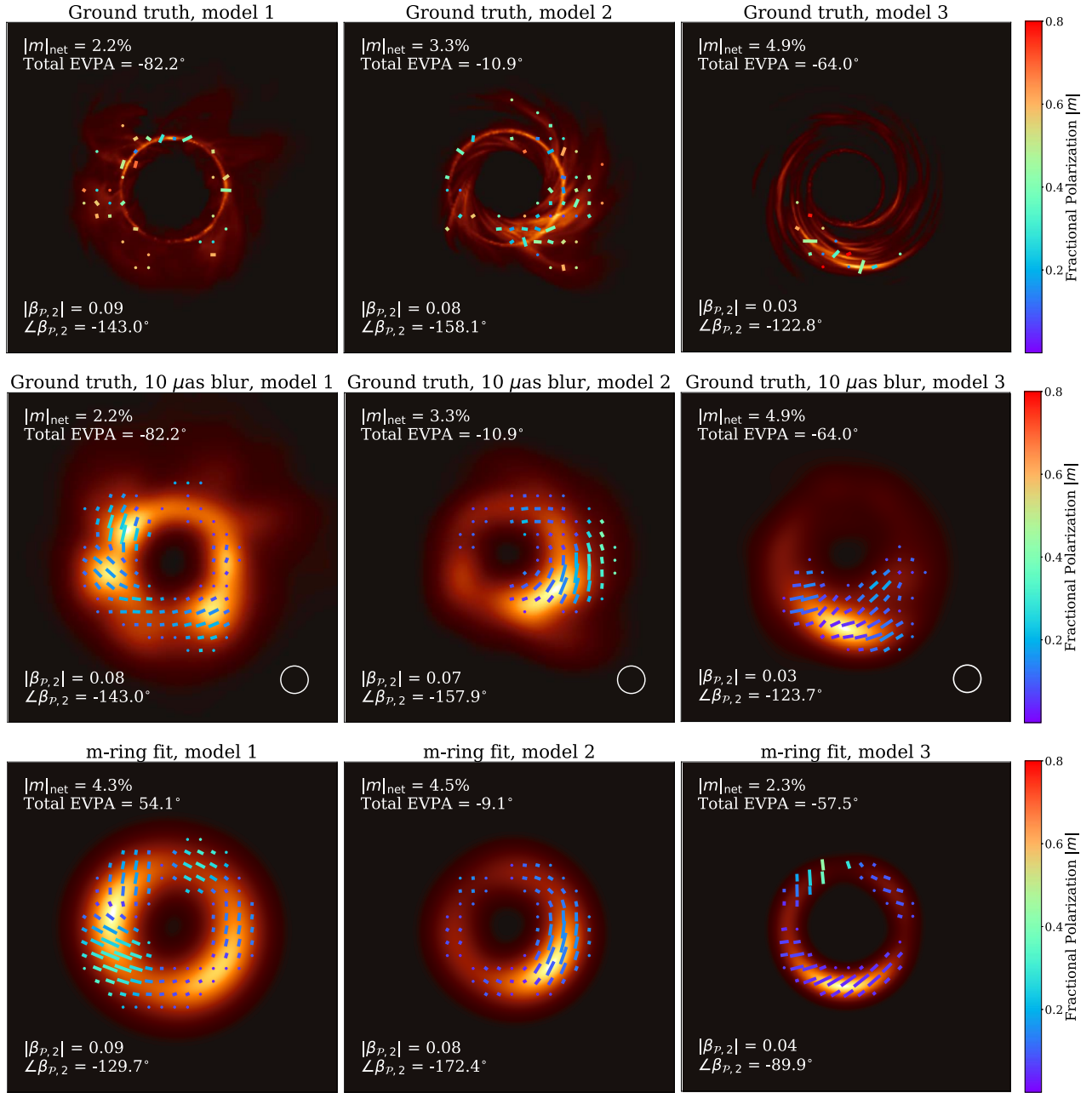


Figure 4. Total intensity and linear polarization reconstructions of our three GRMHD models (left to right), from synthetic data with EHT 2017 coverage. The unblurred and blurred (FWHM $10 \mu\text{as}$) ground-truth images are shown in the top and middle rows, respectively. The bottom row shows the posterior maxima of m-ring fits with $m_{\mathcal{I}} = 3$ and $m_{\mathcal{P}} = 3$. In each panel, the Stokes \mathcal{L} structure is indicated by the heat map, and the scale is normalized to the brightest pixel in each panel. The tick length indicates the polarized intensity, the tick orientation indicates the EVPA, and the tick color indicates the fractional linear polarization. The m-ring fit posteriors for several key parameters are compared to the ranges found by Event Horizon Telescope Collaboration et al. (2019a, 2019d, 2021a) in Table 1.

5.3. Circular Polarization Results

Figure 5 shows the posterior maxima of the Stokes \mathcal{V} m-ring fits to synthetic data from the three GRMHD models. These were produced as outlined in Section 4.2, with the assumption of a perfect leakage calibration. The m-ring model is suitable for recovering the basic, low-order properties of the complex Stokes \mathcal{V} structure in the GRMHD models, although, as for linear polarization, the performance varies depending on the ground-truth model. For model 1, the first-order orientation of the Stokes \mathcal{V} structure, $\angle\beta_{\mathcal{V},1}$, is reproduced to within a few degrees for $m_{\mathcal{V}} = 1$ (see also Figure 6, which shows the complex $\beta_{\mathcal{V},1}$ posteriors compared to the ground-truth values),

and to within 30° – 50° for $m_{\mathcal{V}} = 2$. The $\angle\beta_{\mathcal{V},1}$ of the $m_{\mathcal{V}} = 3$ fit to the visibility ratios deviates most significantly, which is likely due to the multilobe structure of the $m_{\mathcal{V}} = 3$ model in combination with a low total circular polarization fraction, so that a small deviation in one of the lobes can result in a large deviation of the first-order orientation $\angle\beta_{\mathcal{V},1}$.

The Stokes \mathcal{V} structure of model 2 is more complex, but $\angle\beta_{\mathcal{V},1}$ is nevertheless recovered to within less than 40° . The higher m-order fits are more informative here, recovering the alternating regions of positive and negative Stokes \mathcal{V} along the ring.

The Stokes \mathcal{V} structure of model 3 is less ring-like than for the other models, with most of the Stokes \mathcal{V} emission

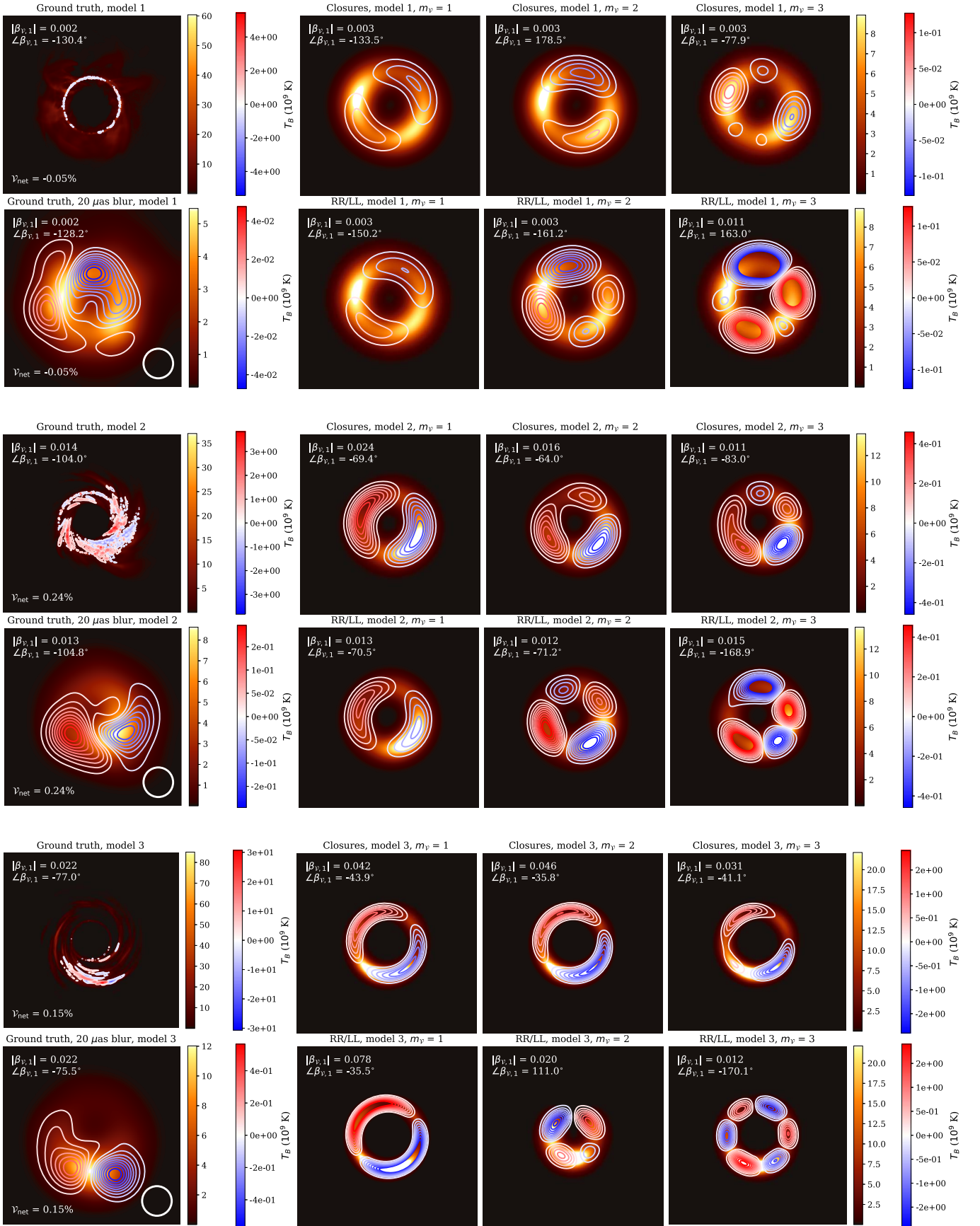


Figure 5. GRMHD ground-truth Stokes \mathcal{V} images and m -ring fits from EHT 2017 April 11 coverage (low band). Each model covers a set of two rows. The left column shows the ground truth without (upper panels) and with (lower panels) Gaussian blurring (FWHM $20 \mu\text{as}$). The right three columns show the Stokes \mathcal{V} m -ring fits for $m_v = 1, 2, 3$, fitting to closure quantities (upper panels for each model) and RR/LL visibility ratios (lower panels for each model).

concentrated in the South. The $\beta_{\mathcal{V},1}$ posteriors (Figure 6) are farther away from the ground truth than for the other models, despite the fact that the image-averaged circular polarization fraction $\langle |\mathcal{V}/\mathcal{I}| \rangle$ is highest for this model. The low m-order fits nevertheless limit the first-order orientation offset to within 30° – 40° . Interestingly, the higher m-order fits to the visibility ratios favor a much smaller ring size in order to capture the compact Stokes \mathcal{V} emission in the South.

To summarize, the m-ring model is able to recover low-order Stokes \mathcal{V} structures for these three quite distinct GRMHD models with varying accuracy. Since the Stokes \mathcal{V} structure is often complex, there are systematics due to model misspecification (the low-order m-ring model does not fully describe the physical characteristics of the Stokes \mathcal{V} emission), but the first-order asymmetry orientation is recovered to within a few tens of degrees for $m_{\mathcal{V}} = 1, 2$. Higher-order m-ring fits perform well if the ground-truth Stokes \mathcal{V} structure is well described by alternating lobes of positive and negative Stokes \mathcal{V} (model 2), but these fits are often less consistent in other cases and hence should be applied with caution in practice. We do not see a clear trend of increasing Stokes \mathcal{V} reproducibility with increasing $\langle |\mathcal{V}/\mathcal{I}| \rangle$ for these data sets. As discussed in Paper IX, imaging methods showed similar and often greater difficulty in recovering the circular polarization structure from these data sets, and m-ring modeling often outperforms imaging in the recovery of quantities like the image-averaged circular polarization fraction or the first-order orientation, especially when the net circular polarization fraction is low. The m-ring modeling is therefore a useful tool for studying low-order circular polarization structures in mm-VLBI observations of black holes.

6. Application to EHT Data of M87*

In this section, we apply our polarimetric m-ring modeling framework to EHT 2017 observations of M87*. We use data calibrated through the EHT HOPS pipeline (Event Horizon Telescope Collaboration et al. 2019c; Blackburn et al. 2019; Event Horizon Telescope Collaboration et al. 2023), unless otherwise specified (Section 6.2). We use both low-band (LO, with a central frequency of 227.1 GHz) and high-band (HI, with a central frequency of 229.1 GHz) data for our analyses. Both bands have a bandwidth of 2 GHz. All data sets were leakage calibrated using the estimated D -terms from Event Horizon Telescope Collaboration et al. (2021a) and Issaoun et al. (2022), which have estimated residual leakages of only $\sim 1\%$. We show our recovery of the previously imaged linear polarization structure (Event Horizon Telescope Collaboration et al. 2021a) in Section 6.1. In Section 6.2, we then show our circular polarization fits to M87* data, providing an extension and more detailed exploration of the fits presented in Paper IX.

6.1. Linear Polarization

Figure 7 shows our total intensity and linear polarization fits ($m_{\mathcal{I}} = 3, m_{\mathcal{P}} = 3$) to EHT 2017 M87* data on 4 days (April 5, 6, 10, and 11), with and without blurring the images with a Gaussian kernel with an FWHM of $20 \mu\text{as}$. This blurring kernel is representative for the blurring kernels used for the images in Event Horizon Telescope Collaboration et al. (2019d) and Event Horizon Telescope Collaboration et al. (2021a). Table 1 compares our fitted parameters to previous EHT results (Event Horizon Telescope Collaboration et al. 2019a, 2019d,

2019f, 2021a). The structure recovered with our m-ring fits is remarkably consistent across days and in excellent agreement with previous EHT imaging and modeling results, especially when our fits are blurred.

For consistency with Event Horizon Telescope Collaboration et al. (2019a), we report the shifted diameter

$$d' = d - \frac{1}{4 \ln 2} \frac{\alpha^2}{d} \quad (14)$$

in Table 1. This shifted diameter accounts for the change in peak brightness radius for a thick ring with FWHM α as compared to an infinitesimally thin ring (Event Horizon Telescope Collaboration et al. 2019d). The diameter change is of order $2 \mu\text{as}$ for the values reported in Table 1.

For a blurring kernel with FWHM W , the change in ring thickness can be approximated as (Event Horizon Telescope Collaboration et al. 2019d)

$$\alpha_{\text{blur}} \approx \sqrt{\alpha^2 + W^2}. \quad (15)$$

For the blurred m-ring posterior ranges reported in Table 1 (fifth column), our α -posteriors were transformed following this approximation, with $W = 20 \mu\text{as}$. These values were then used to compute the blurred d' posterior ranges following Equation (15). The β -values for the blurred fits were computed by generating 1000 image samples from the posteriors, blurring them with a $20 \mu\text{as}$ beam, and computing the values from the blurred image samples. Most fitted quantities are insensitive or only weakly sensitive to image blurring. An exception is $|\beta_{\mathcal{P},2}|$, which reduces significantly after blurring.

As found in the previous EHT analyses, the peak brightness in total intensity moves from the southeast toward the southwest for the later days. The total linear polarization between about 1.5% and 4.3% is consistent, within error bars, with that recovered by the polarimetric imaging methods in Event Horizon Telescope Collaboration et al. (2021a), which reported values between 1.0% and 3.7%. Our fitted $\angle\beta_{\mathcal{P},2}$ between about -136° and -121° is also in agreement with the EHT imaging results, which reported values between -163° and -127° (except for a slight offset for the fit to high-band data on April 6). There is a significant discrepancy for $|\beta_{\mathcal{P},2}|$, but as shown in Figure 7 and Table 1, this quantity is sensitive to the applied blurring kernel, and the values are in full agreement when blurring our models with a $20 \mu\text{as}$ Gaussian kernel. Our posterior widths (Table 1) are generally much smaller than the ranges spanned by the EHT imaging methods, indicating that systematic offsets (model misspecifications) are likely dominant over the statistical uncertainties from fitting a specific model to the data. For all quantities, the statistical uncertainty is largest for April 10 data, which indeed has the smallest number of M87* scans (amounting to less than 30 minutes on-source).

6.2. Circular Polarization

6.2.1. Fit Results

Figure 8 shows our circular polarization m-ring fits of EHT M87* data on April 5, 6, 10, and 11. Figure 9 shows complete polarization ellipse plots for the same fits, which include total intensity, linear, and circular polarization information. Corresponding posterior ranges are reported in Table 1. These figures and table represent fits with an $m_{\mathcal{V}} = 1$ m-ring to closure

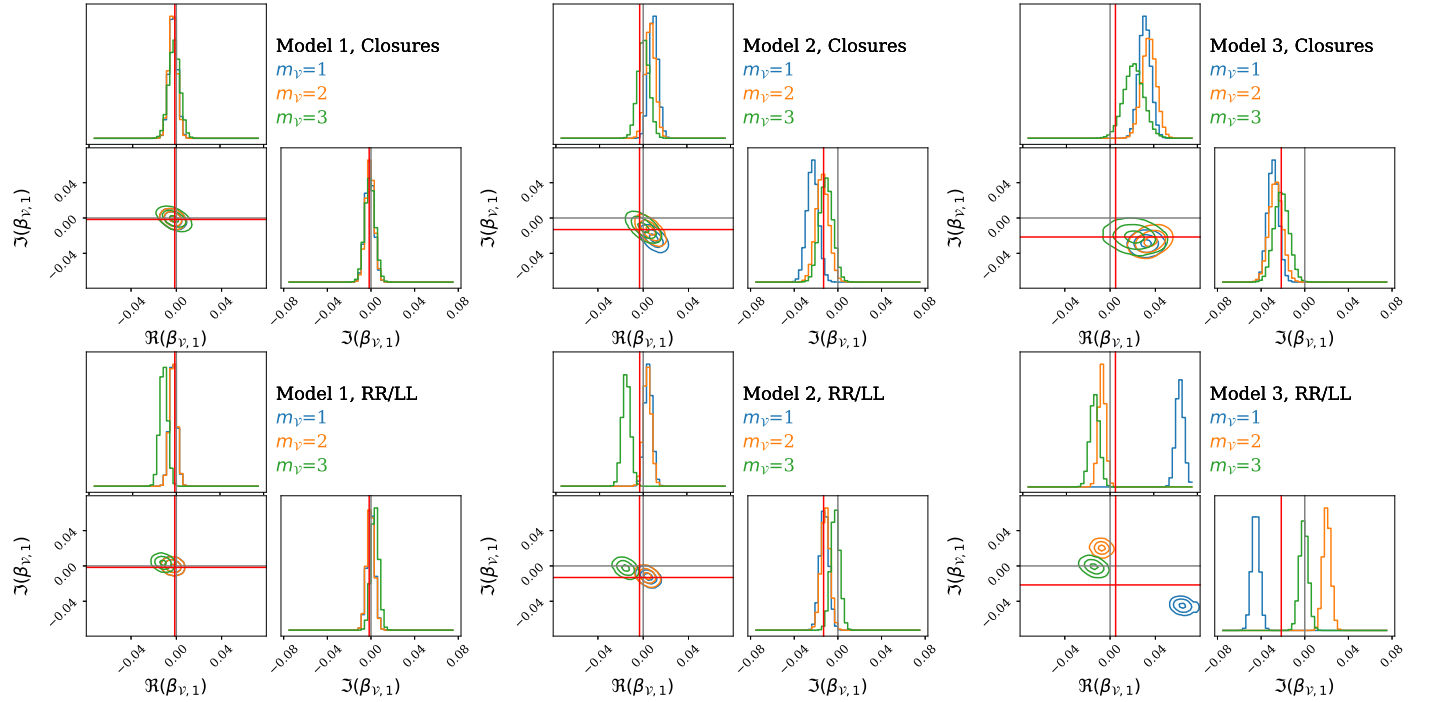


Figure 6. $\beta_{\nu,1}$ posteriors for the Stokes \mathcal{V} m-ring fits to closure quantities (top row) and *RR/LL* visibility ratios (bottom row) from synthetic observations (EHT 2017 April 11, low band) of our GRMHD models 1, 2, and 3 (left to right). The contours show 1σ , 2σ , and 3σ levels. The red lines indicate the ground-truth values.

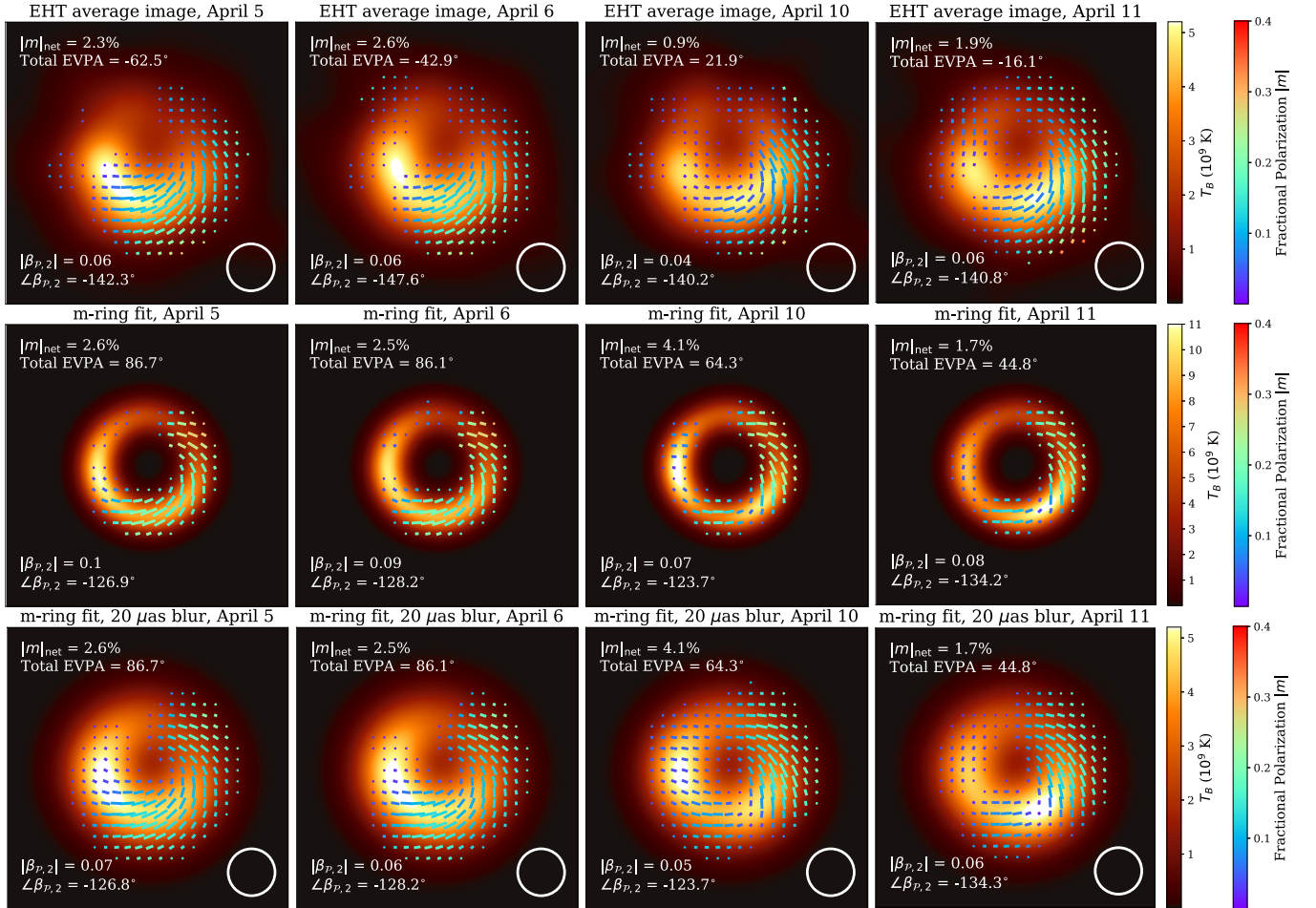


Figure 7. EHT 2017 method-averaged total intensity and linear polarization images of M87* (top row; Event Horizon Telescope Collaboration et al. 2021a) on April 5, 6, 10, and 11 (left to right), compared to our total intensity and linear polarization m-ring fits (posterior maxima; $m_T = 3$, $m_P = 3$) to the same data, without (middle row) and with (bottom row) blurring with a Gaussian kernel with an FWHM of $20 \mu\text{as}$.

Table 1

Parameters Describing the Total Intensity and Polarization Structure of M87* as Observed by the EHT in 2017 Extracted through Imaging and Crescent Fitting (Event Horizon Telescope Collaboration et al. 2019a, 2019d, 2021a) and m-ring Fitting (This Work)

Parameter	Day	EHTC Imaging + Modeling	m-ring Fitting LO	m-ring Fitting H I	m-ring Fitting LO, 20 μ as blur	m-ring Fitting H I, 20 μ as blur
d' (μ as)	Apr 5	42 ± 3^a	42.07 ± 0.56	41.261 ± 0.68	38.74 ± 0.60	38.27 ± 0.73
	Apr 6		42.25 ± 0.43	42.52 ± 0.58	38.93 ± 0.54	39.25 ± 0.62
	Apr 10		43.24 ± 0.91	43.53 ± 0.94	39.98 ± 0.97	40.32 ± 0.94
	Apr 11		43.53 ± 0.47	43.01 ± 0.33	40.30 ± 0.50	39.72 ± 0.39
α (μ as)	Apr 5	$<20^a$	12.31 ± 0.78	13.71 ± 0.79	23.49 ± 0.41	24.25 ± 0.45
	Apr 6		12.16 ± 0.69	13.68 ± 0.61	23.41 ± 0.36	24.23 ± 0.61
	Apr 10		11.04 ± 1.26	13.28 ± 0.98	22.85 ± 0.60	24.01 ± 0.54
	Apr 11		11.97 ± 0.67	12.48 ± 0.60	23.22 ± 0.34	23.57 ± 0.32
$ \beta_{\mathcal{I},1} $	Apr 5	$0.16\text{--}0.32^b$	0.197 ± 0.010	0.208 ± 0.013	0.171 ± 0.008	0.176 ± 0.011
	Apr 6		0.203 ± 0.009	0.215 ± 0.011	0.178 ± 0.007	0.184 ± 0.008
	Apr 10		0.138 ± 0.015	0.155 ± 0.018	0.121 ± 0.013	0.134 ± 0.014
	Apr 11		0.166 ± 0.012	0.172 ± 0.012	0.138 ± 0.010	0.141 ± 0.009
$\angle\beta_{\mathcal{I},1}$ (deg)	Apr 5	$-200\text{--}150^a$	-139.2 ± 4.3	-145.1 ± 4.9	-134.3 ± 4.4	-140.4 ± 5.2
	Apr 6		-141.8 ± 3.95	-144.2 ± 4.1	-137.0 ± 4.0	-139.8 ± 4.3
	Apr 10		-137.4 ± 11.9	-139.3 ± 10.6	-130.6 ± 12.4	-133.6 ± 11.1
	Apr 11		-172.3 ± 3.7	-174.6 ± 3.4	-167.8 ± 4.2	-170.2 ± 3.7
$ m _{\text{net}}$ (%)	Apr 5	$1\text{--}3.7^c$	2.51 ± 0.61	2.40 ± 0.64	2.51 ± 0.61	2.40 ± 0.64
	Apr 6		2.53 ± 0.50	2.51 ± 0.50	2.53 ± 0.50	2.51 ± 0.50
	Apr 10		4.25 ± 0.88	3.38 ± 0.87	4.25 ± 0.88	3.38 ± 0.87
	Apr 11		1.68 ± 0.51	1.46 ± 0.49	1.68 ± 0.51	1.46 ± 0.49
$ \beta_{\mathcal{P},2} $	Apr 5	$0.04\text{--}0.07^c$	0.110 ± 0.006	0.110 ± 0.007	0.068 ± 0.004	0.065 ± 0.004
	Apr 6		0.103 ± 0.006	0.106 ± 0.006	0.063 ± 0.004	0.064 ± 0.004
	Apr 10		0.084 ± 0.011	0.080 ± 0.012	0.053 ± 0.007	0.050 ± 0.008
	Apr 11		0.090 ± 0.007	0.090 ± 0.007	0.058 ± 0.005	0.057 ± 0.004
$\angle\beta_{\mathcal{P},2}$ (deg)	Apr 5	$-163\text{--}127^c$	-126.2 ± 3.3	-128.1 ± 3.7	-125.8 ± 3.3	-128.0 ± 3.7
	Apr 6		-129.4 ± 3.3	-123.0 ± 3.4	-129.0 ± 3.2	-122.8 ± 3.3
	Apr 10		-125.5 ± 7.7	-121.4 ± 8.9	-126.0 ± 7.9	-122.2 ± 9.0
	Apr 11		-135.7 ± 4.5	-133.3 ± 4.6	-136.3 ± 4.4	-134.0 ± 4.5
$ \beta_{\mathcal{V},1} $	Apr 5	$\lesssim 0.02^d$	0.013 ± 0.008	0.010 ± 0.009	0.011 ± 0.007	0.009 ± 0.008
	Apr 6		0.013 ± 0.010	0.012 ± 0.007	0.012 ± 0.008	0.010 ± 0.006
	Apr 10		0.024 ± 0.018	0.007 ± 0.014	0.021 ± 0.016	0.005 ± 0.012
	Apr 11		0.022 ± 0.010	0.016 ± 0.009	0.019 ± 0.009	0.014 ± 0.008
$\angle\beta_{\mathcal{V},1}$ (deg)	Apr 5	$\sim -90\text{--}180^d$	12.01 ± 45.4	6.7 ± 66.7	13.1 ± 45.5	2.2 ± 43.9
	Apr 6		-28.0 ± 36.6	13.7 ± 50.9	-27.7 ± 36.6	14.9 ± 50.5
	Apr 10		-30.0 ± 37.0	-33.2 ± 138.2	-29.7 ± 37.4	-30.8 ± 149.4
	Apr 11		-27.8 ± 17.4	-25.9 ± 25.3	-27.7 ± 18.0	-26.2 ± 24.4
$\langle \mathcal{V}/\mathcal{I} \rangle$ (%)	Apr 5	$<3.7^d$	1.7 ± 1.0	1.5 ± 1.1	1.5 ± 0.9	1.3 ± 1.0
	Apr 6		1.7 ± 1.1	1.6 ± 0.9	1.5 ± 1.0	1.4 ± 0.8
	Apr 10		3.0 ± 2.2	1.4 ± 1.6	2.8 ± 2.0	1.3 ± 1.5
	Apr 11		2.8 ± 1.2	2.1 ± 1.1	2.5 ± 1.1	1.9 ± 1.0

Notes. The fitted model has $m_{\mathcal{I}} = 3$, $m_{\mathcal{P}} = 3$, and $m_{\mathcal{V}} = 1$, with circular polarization fits to closure quantities. The m-ring fit values indicate the posterior means with 2σ ranges. The $\langle|\mathcal{V}/\mathcal{I}|\rangle$ values were computed from posterior image samples. The blurred m-ring parameters were obtained by propagation of the fit posteriors for d' , α , and $|m|_{\text{net}}$, and from blurred image samples for the β parameters and $\langle|\mathcal{V}/\mathcal{I}|\rangle$ (see text for further details).

^a Event Horizon Telescope Collaboration et al. (2019a).

^b Event Horizon Telescope Collaboration et al. (2019d).

^c Event Horizon Telescope Collaboration et al. (2021a).

^d Paper IX.

products; fits with varying Stokes \mathcal{V} m-ring order and fits to RR/LL visibility ratios are explored in Figures 10 and 11. Our fits identify a first-order (dipolar) circular polarization asymmetry that is broadly consistent across the four observing epochs spanning a

6-day window, with more negative Stokes \mathcal{V} in the south and more positive Stokes \mathcal{V} in the north. The strength of the dipolar asymmetry slightly increases toward the later epochs, as indicated by the increase in $|\beta_{\mathcal{V},1}|$ and $\langle|\mathcal{V}/\mathcal{I}|\rangle$. The closure-only fit to the

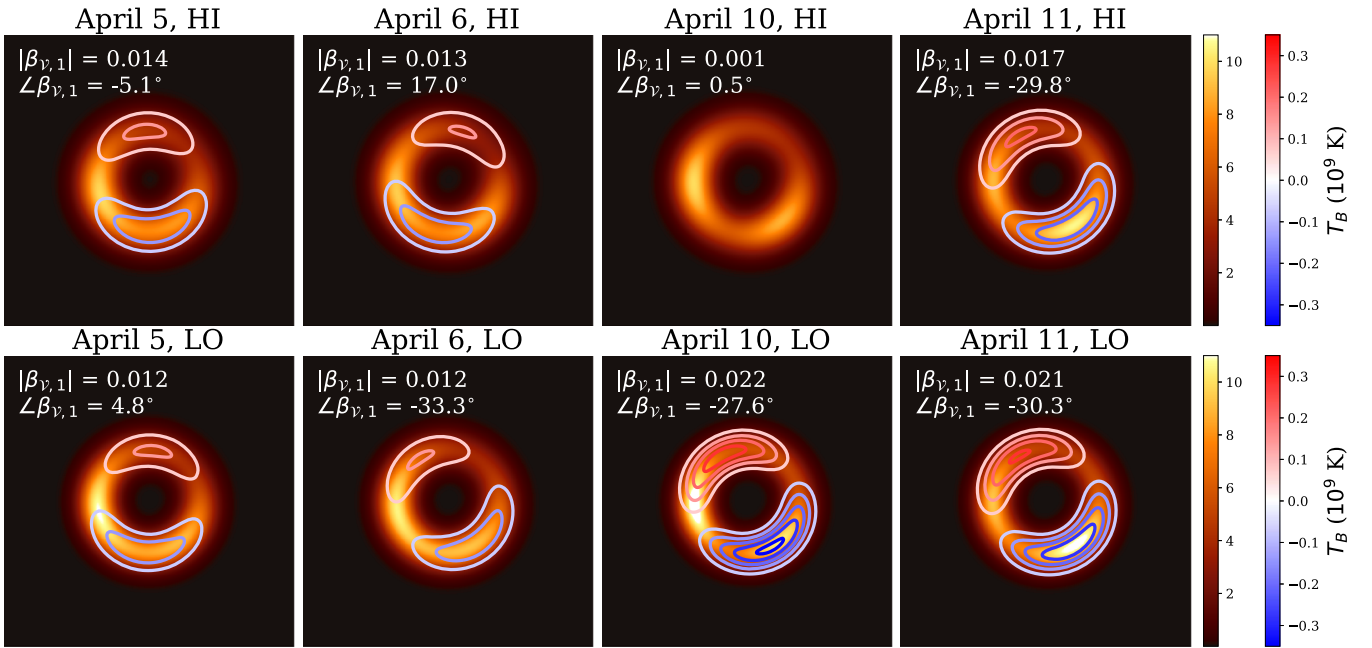


Figure 8. Circular polarization m-ring fits ($m_\nu = 1, m_\tau = 3$; posterior maxima) to closure products of low-band EHT 2017 M87* data on April 5, 6, 10, and 11 (left to right). The heat map indicates the Stokes \mathcal{I} structure, and the contours indicate the Stokes \mathcal{V} structure. These fits are also presented in Paper IX.

April 10 high-band data is an outlier; the $\beta_{\nu,1}$ posterior is too broad for significant dipole structure to be detected (Table 1).

As shown in Figure 10, the overall Stokes \mathcal{V} morphology of the fits is remarkably consistent between fitting to different data products and fitting an $m_\nu = 1$ or $m_\nu = 2$ model, on all days. This consistency starts to break down for $m_\nu = 3$, although it persists for fits using data from April 10 and 11, where the asymmetry for the low m-order fits is most prominent.

The $\beta_{\nu,1}$ posteriors in Figure 11 indicate that a significant dipolar signal is found by nearly all our fits, since $\beta_{\nu,1}$ is nonzero at a $>3\sigma$ level, especially for the $m_\nu = 1$ and $m_\nu = 2$ fits. The posteriors are generally broader for the closure-only fits. The posteriors also indicate a preferred $\beta_{\nu,1}$ orientation close to the positive real axis, indeed corresponding to positive Stokes \mathcal{V} in the north.

Considering the Bayesian evidence $\ln \mathcal{Z}$ and reduced χ^2 as shown in Figure 12, the preferred Stokes \mathcal{V} m-ring order depends on the data product, day, and band that is fit. For the closure-only fits, the Bayesian evidence mostly decreases and the goodness of fit remains approximately equal toward higher m_ν , indicating a preference for a low-order m-ring. Interestingly, $\ln \mathcal{Z}$ is larger for $m_\nu = 1$ than for $m_\nu = 0$ for the April 11 low-band fit ($m_\nu = 0$ corresponds to constant \mathcal{V} along the ring), while the $m_\nu = 1$ values are slightly lower for the other data sets. Additionally, the $\beta_{\nu,1}$ posteriors (Figure 11) are farthest from zero compared to the other days. These trends indicate that the evidence for the presence of dipolar circular polarization structure is largest for April 11 (especially low band).

For the fits to visibility ratios, the Bayesian evidence mostly increases and the χ^2 decreases toward higher m_ν , indicating a preference for higher-order m-rings. The difference in Bayesian evidence is especially large between $m_\nu = 0$ and $m_\nu = 1$ on April 6 and 11, which is a strong indicator of the presence of horizon-scale Stokes \mathcal{V} structure. The Bayesian evidence peaks at $m_\nu = 1$ for April 6 and 11 (low band), indicating a preference for a dipole structure. Considering the increased

inconsistency among the fit Stokes \mathcal{V} structure for $m_\nu = 3$ (Figure 10), the same trends occurring in our GRMHD fits, and the fact that the visibility ratio fits could be affected by R/L gain calibration uncertainties, we have presented the closure-only $m_\nu = 1$ fits as the main modeling result in Paper IX. We do not deem any further fitted substructure trustworthy. The $m_\nu = 3$ fits to visibility ratios may be picking up on smaller-scale structure that the lower-order m-rings cannot account for, but in some of our GRMHD tests we have seen that these fits may present images that do not correctly reproduce this smaller-scale structure (Figure 5). Future EHT data sets with better uv -coverage and sensitivity will allow us to detect circular polarization structure more strongly and in more detail than these first-order structure results.

Figure 13 shows that the basic structure of the posterior maxima is independent of the assumed \mathcal{V}_{net} , within the range reported from ALMA-only measurements by Goddi et al. (2021).

6.2.2. Sensitivity to R/L Gain Calibration Strategy

As noted in Section 3.1, the RR/LL visibility ratio data product is affected by nonunity R/L gain ratios, while the parallel-hand closure data products are not. In this section, we explore the sensitivity of our M87* fit results to the gain calibration strategy. The R/L gain ratios in the HOPS data (used in Sections 6.1 and 6.2.1) were calibrated by fitting a polynomial to the RR and LL visibility offsets (amplitude ratios and phase differences) as a function of time for 10 sources observed during the 5 days of the 2017 EHT campaign. By using data from multiple sources and days, circular polarization signatures of individual sources (assumed to be independent and thus averaged out) could be separated from instrumental R/L gain offsets (shared between the sources). The visibility differences could be fit with a constant complex gain ratio for all stations, except for APEX and SMA, which showed stronger time dependence of the RR and LL visibility phase differences and hence required a time-dependent polynomial fit for the R/L gain phases. Some more details are

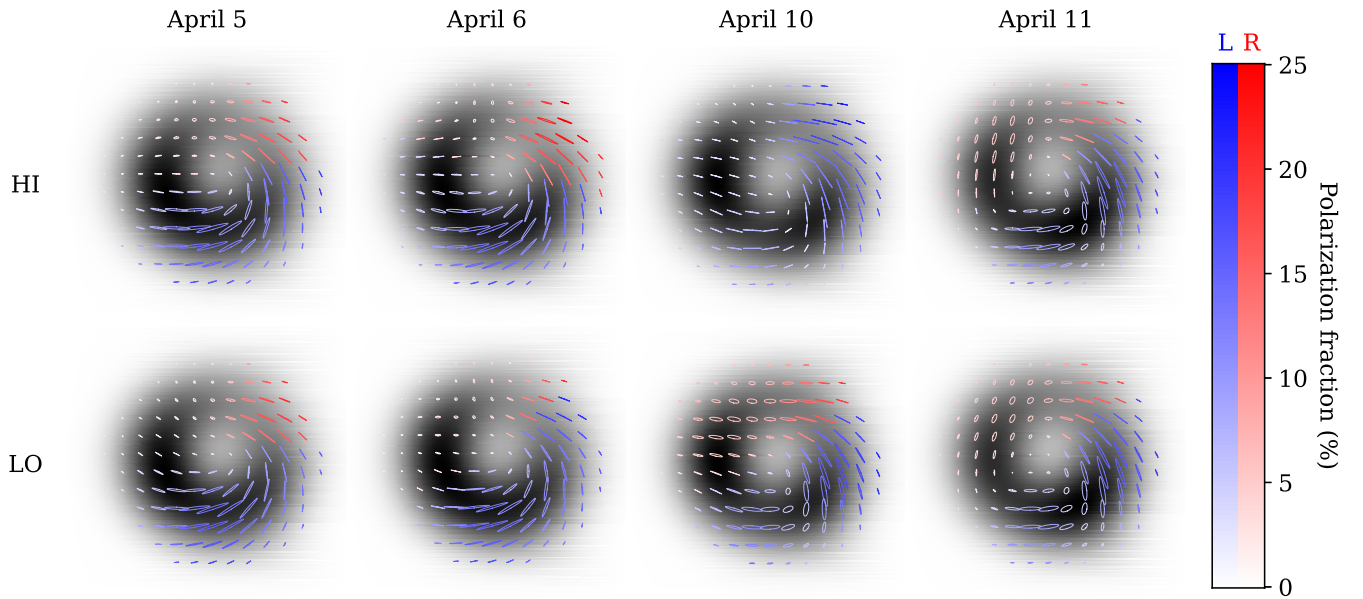


Figure 9. Polarization ellipse plots of our polarimetric m-ring model fits shown in Figure 8, blurred with a $20 \mu\text{as}$ Gaussian beam. The total intensity structure is indicated in gray scale, and the ellipses indicate the total polarization $\sqrt{Q^2 + U^2 + V^2}/I$. The ellipse sizes are proportional to the total polarized brightness, the orientations indicate the linear polarization EVPA, the ellipticities indicate the circular polarization fraction, and the colors indicate the circular polarization sign and fraction. Posterior means for the April 11 fits are presented in the same format in Paper IX.

given in Paper IX, with an illustration of an R/L phase fit shown in Figure 14 therein, indicating a well-behaving set of sources, without any strongly polarized outlier. The general similarity of our RR/LL fits to our closure-only fits (Figure 10) can be taken as an indication that the effect of any residual R/L gain ratios on our fits is limited.

The robustness of our RR/LL fits in particular can also be tested in an exercise where we attempt to remove the circular polarization signal by self-calibrating the R and L gains separately to our total intensity model assuming $\mathcal{V} = 0$, before fitting the Stokes \mathcal{V} structure (e.g., Homan & Wardle 2004). Figure 14 shows the result of performing such an exercise on the EHT HOPS data. Here we have set a solution interval of 2 hr for both the gain amplitudes and gain phases. As expected, the closure-only fits are unaffected by this operation, since the closure products are robust against station gains. The RR/LL fits are clearly affected, showing substantially weaker circular polarization structure (note the difference in scale between the two rows) and a different orientation on most days. The exception is April 11, where the zero- \mathcal{V} self-calibration failed to remove the dipole structure with approximately north–south orientation, although it is substantially weaker.

To test the sensitivity of our model fitting procedure to upstream calibration choices, we also fit our polarimetric m-ring model to a new version of the 2017 EHT data, which has been calibrated in a slightly different way. We utilize the CASA-VLBI-based (van Bemmelen et al. 2022) $rPICARD$ (Janssen et al. 2019) pipeline to solve for instrumental offsets (Event Horizon Telescope Collaboration et al. 2019c) and then combine the two LO plus HI frequency bands and all polarization correlation products to solve for fringes and atmospheric phases (M. Janssen et al. 2023, in preparation). In contrast to the multisource polynomial fit R/L gain calibration described above, either no R/L amplitude gain ratios are applied to the CASA data used here, or an R/L gain amplitude ratio calibration was performed assuming zero circular polarization.

Figure 15 shows the polarimetric modeling results of the new CASA data. As expected, the R/L gain-insensitive closure-based fitting is in excellent agreement with the HOPS data results. Even without any R/L gain calibration or assuming $\mathcal{V} = 0$, consistent circular polarization signals are retrieved here. However, for the RR/LL visibility ratio fits, the differences in Stokes \mathcal{V} structures with the HOPS results and the inconsistency between observing epochs demonstrate a significant sensitivity to the R/L gain calibration strategy (since these are posterior maxima, the structure itself does not look more noisy than for the HOPS data). For April 11 data, on which the HOPS fits indicated the strongest evidence for the presence of dipolar Stokes \mathcal{V} structure, the CASA RR/LL fits are in agreement with the closure and HOPS data fits regardless of the R/L gain calibration strategy, which may indicate a reduced sensitivity to R/L gains due to the stronger Stokes \mathcal{V} signal on this day.

The consistency of the results with the previously used, well-validated, 2017 calibrated EHT data demonstrates the robustness of our method relative to different calibration assumptions and serves as a first validation of the updated CASA/ $rPICARD$ data reduction pathway. Our fits across different data sets, data products, and modeling assumptions support the presence of a persistent dipolar asymmetry in the circular polarization of M87*, especially on April 11, where this asymmetry persists in the RR/LL fits regardless of calibration strategy.

7. Summary and Outlook

In this work, we have developed a novel method to reconstruct polarimetric image structure from VLBI observations, making use of data products with different levels of calibration invariance and simple geometric models. Specifically, polarimetric m-ring fitting is a useful method to obtain information on the polarimetric structure of horizon-scale observations of supermassive black holes. We have shown that ground-truth polarization parameters can be recovered from

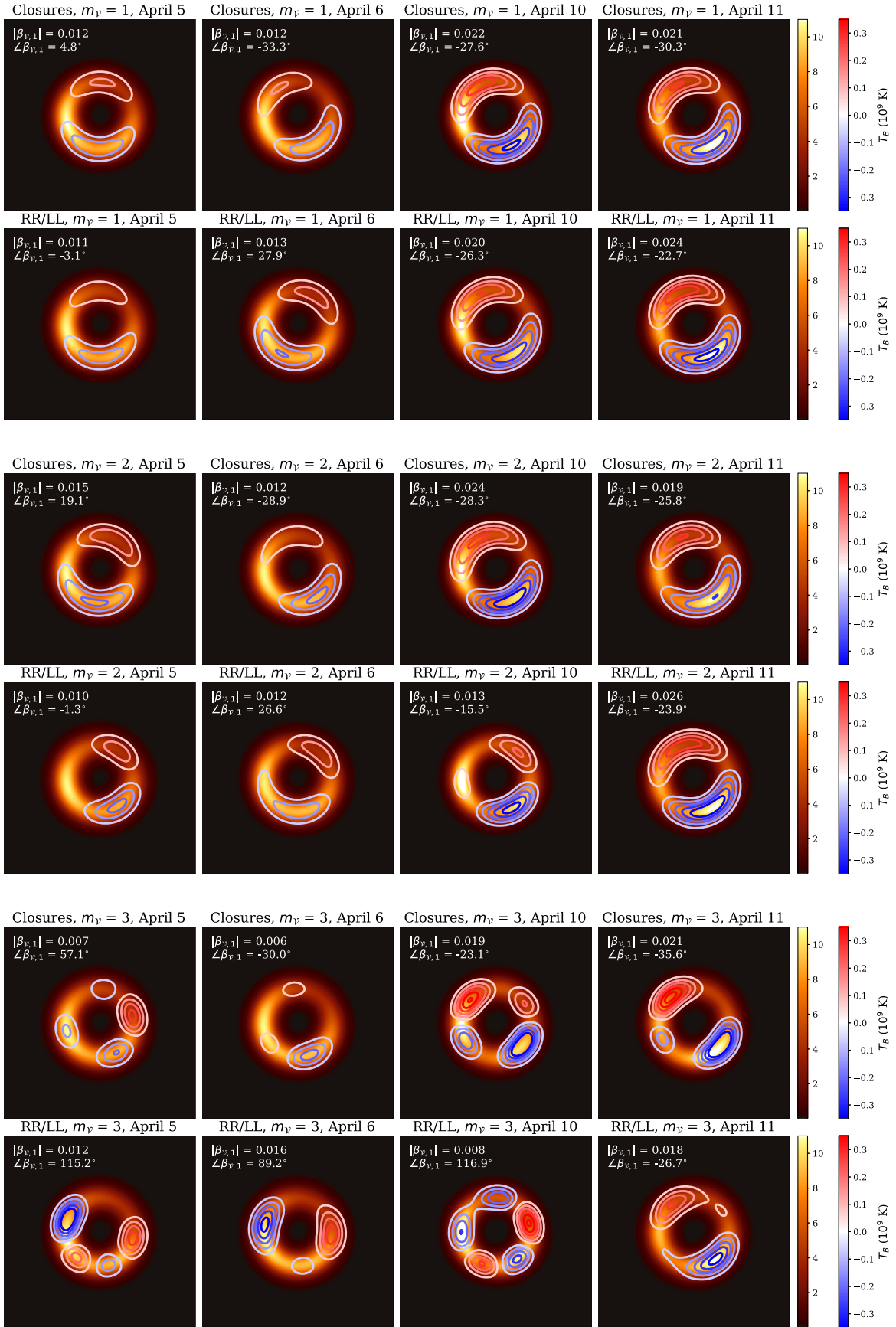


Figure 10. Circular polarization m-ring fits (posterior maxima) to low-band EHT 2017 M87* data on April 5, 6, 10, and 11 (left to right). The three sets of two rows show fits with $m_y = 1, 2, 3$, fitting to closure quantities (upper panels for each m -order) and RR/LL visibility ratios (lower panels for each m -order). The top row panels correspond to the top row panels in Figure 8.

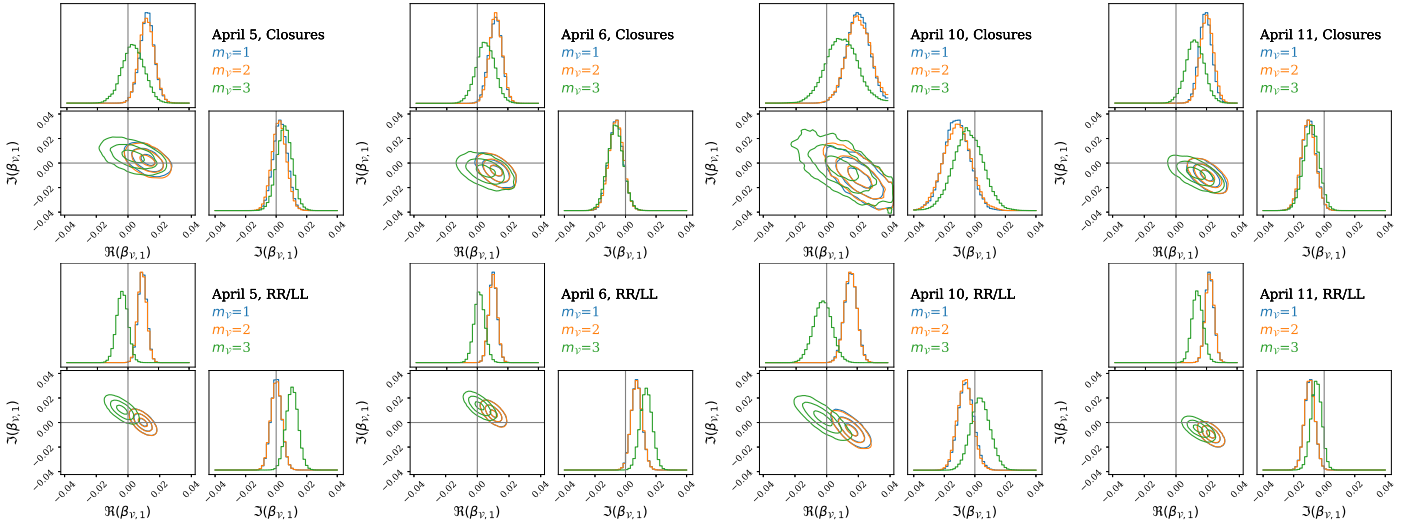


Figure 11. $\beta_{V,1}$ posteriors for the Stokes \mathcal{V} m-ring fits to closure quantities (top row) and RR/LL visibility ratios (bottom row) from low-band EHT 2017 M87* data on April 5, 6, 10, and 11 (left to right). The contours show 1σ , 2σ , and 3σ levels.

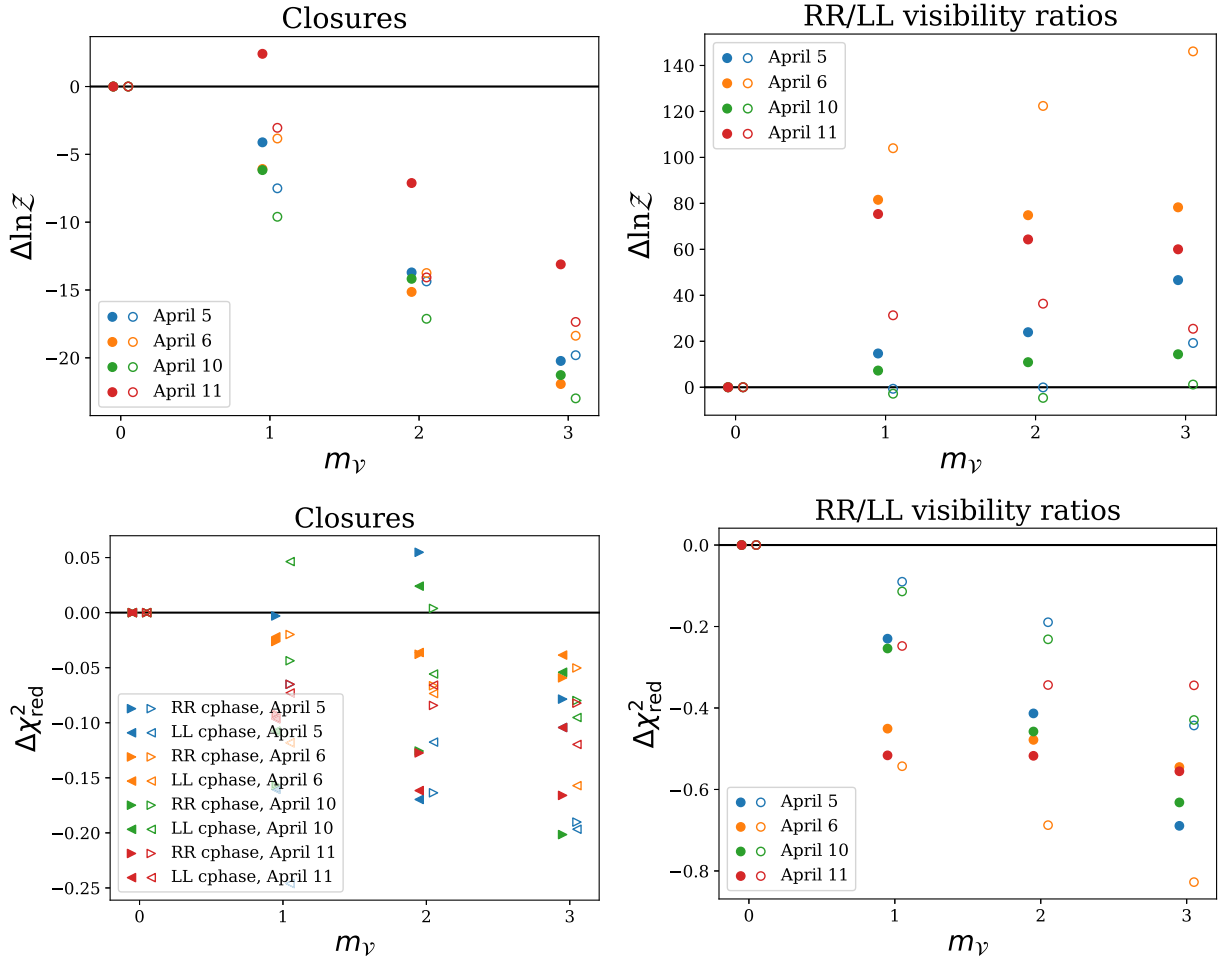


Figure 12. Relative Bayesian evidence (top panels) and reduced χ^2 (bottom panels) as a function of Stokes \mathcal{V} m-ring order m_γ , for the EHT M87* m-ring fits shown in Figures 10 and 11. Low-band fits are indicated with filled symbols, and high-band fits are indicated with open symbols. All values are relative to the $m_\gamma = 0$ fit on each day and band.

synthetic EHT data from geometric m-ring models and GRMHD models, with accuracies depending on the level of model misspecification. Even with total and resolved circular polarization fractions as low as 0.5%, the first-order circular

polarization asymmetry can be recovered from GRMHD models to within a few to $\sim 30^\circ$ – 40° , depending on the model. Polarized structure is recovered most faithfully in image regions with high total intensity.

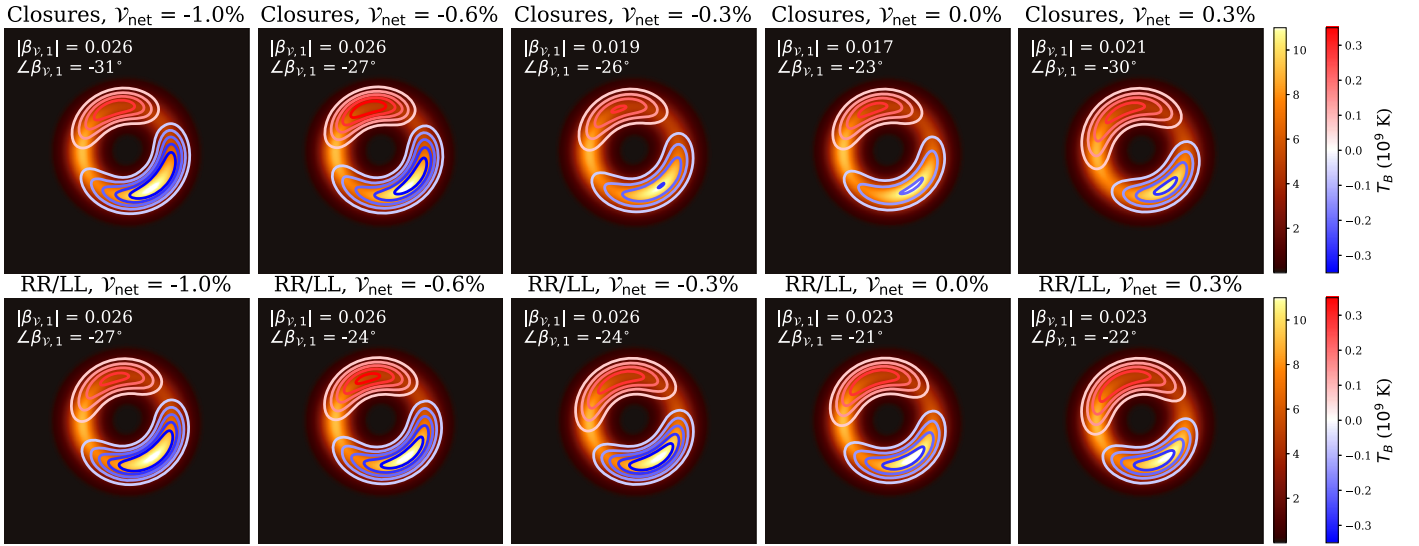


Figure 13. Circular polarization m-ring fits ($m_\nu = 2$, posterior maxima) to EHT 2017 M87* data on April 11, assuming different total circular polarization fractions γ_{net} that span the range reported by Goddi et al. (2021) (left to right). The top row shows fits to closure quantities, and the bottom row shows fits to *RR/LL* visibility ratios.

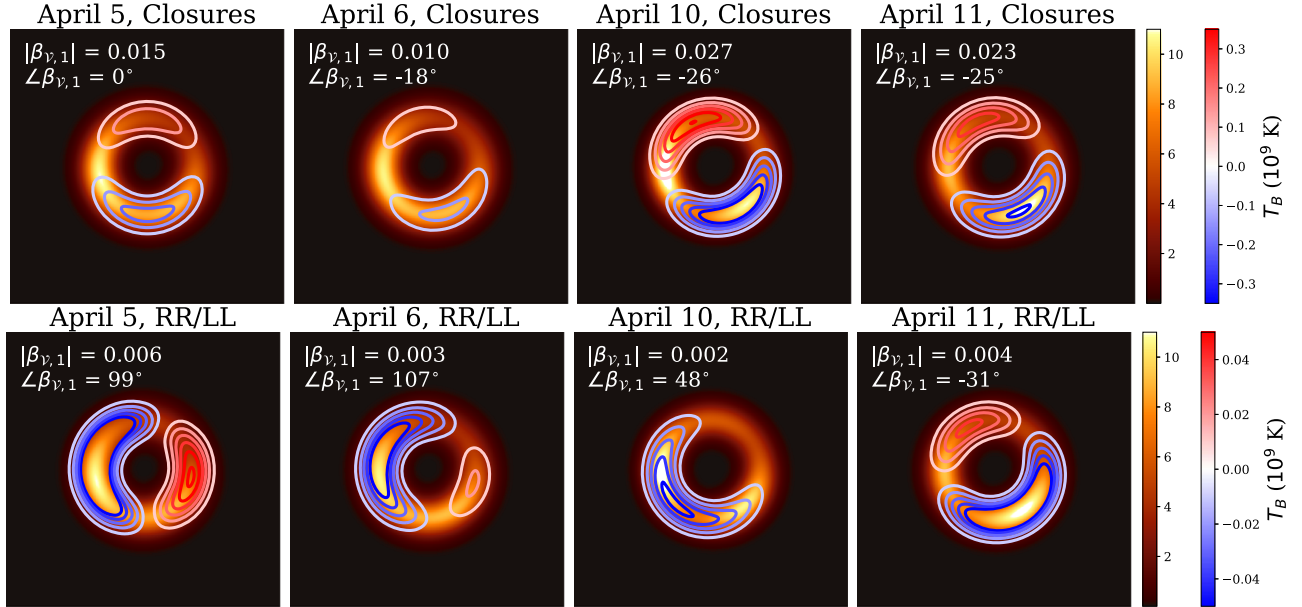


Figure 14. Circular polarization m-ring fits (low band, $m_\nu = 1$, posterior maxima) to EHT 2017 M87* data, performed after self-calibrating the *R* and *L* gains to the total intensity fit assuming $\nu = 0$. The top row shows fits to closure quantities, and the bottom row shows fits to *RR/LL* visibility ratios.

Application to EHT M87* data has shown that the linear polarization structure imaged by Event Horizon Telescope Collaboration et al. (2021a) is recovered well with our m-ring modeling framework. Our fits also indicate the presence of a persistent horizon-scale circular polarization asymmetry, with increased negative circular polarization in the south, near the total intensity maximum. This asymmetry persists across fits to different observing epochs, bands, and data products, across fits with circular polarization m-ring orders m_ν of 1 and 2, for fits assuming different image-integrated circular polarization fractions, and for fits to data calibrated with different calibration pipelines and strategies. Support for the presence of the asymmetry is largest for April 11 data. For this day, a dipolar structure is favored by the Bayesian evidence. Furthermore, for this day, the dipolar structure persists in fits up to $m_\nu = 3$, and in *R/L* gain-sensitive *RR/LL* visibility ratio fits regardless of the

R/L gain calibration strategy used. Some imaging methods reconstruct similar structure on this day (Paper IX).

However, given the overall weakness of the circular polarization signal, the sensitivity of our *RR/LL* fit results to the *R/L* gain calibration strategy on 3 days, and the difficulty for imaging methods to reconstruct similarly consistent structure, caution should be exercised in interpreting this result, and we are not reporting an unambiguous detection of dipolar structure with a specific orientation. While m-ring fitting reliably reconstructed the first-order circular polarization asymmetry in our GRMHD synthetic data tests (with an orientation offset of a few degrees up to $\sim 40^\circ$), there is no guarantee that the underlying circular polarization structure of M87* has a strong dipolar component. Even for a strong asymmetry detection, GRMHD models show degeneracies in black hole and plasma parameters that may produce such

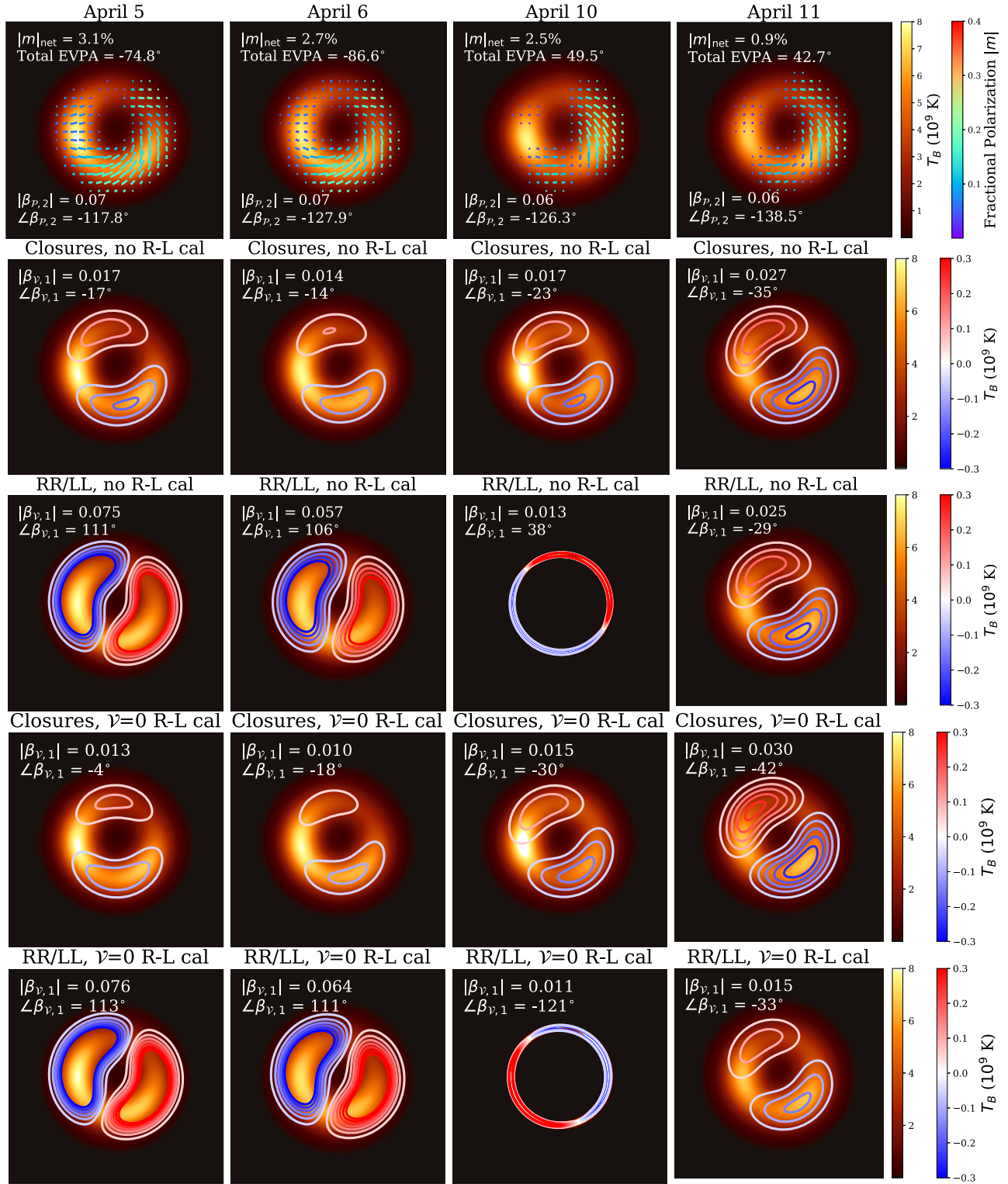


Figure 15. Full Stokes m-ring fits (posterior maxima) to low-band 2017 EHT M87* data, calibrated with the CASA/ ϵ PICARD EHT calibration pipeline (Event Horizon Telescope Collaboration et al. 2019c; Janssen et al. 2019). Rows from top to bottom show linear polarization fits, circular polarization fits to closure quantities without any R/L gain ratio calibration, circular polarization fits to RR/LL visibility ratios without any R/L gain ratio calibration, and circular polarization fits to the same data with an R/L gain ratio calibration assuming $\nu = 0$. The fits shown in the leftmost and rightmost panels of the fourth row are also presented in Paper IX.

asymmetry, and it may be short-lived owing to plasma variability.

As more stations are added to the EHT and antenna sensitivity improves, the circular polarization structure of M87* will become easier to detect and reconstruct. While the

EHT 2017 data only provide upper limits on the resolved circular polarization fraction and tentative circular polarization images with large uncertainties, the future prospects for imaging and modeling M87* in circular polarization are excellent.

Finally, our modeling methods have other applications as well. Apart from fitting horizon-scale structure with m-rings, polarimetric geometric modeling with different model prescriptions (e.g., a set of polarized Gaussians) may also be used to reconstruct the polarized structure of nonhorizon active galactic nuclei. For Sgr A*, snapshot geometric modeling (i.e., fitting to short time snippets of data and then combining the posteriors; Event Horizon Telescope Collaboration et al. 2022d) can utilize our polarimetric m-ring model to mitigate the rapid source variability and constrain the polarimetric structure with only a small number of baselines. With future arrays with many more stations, such as the Next-Generation EHT (ngEHT; Doeleman et al. 2019, 2023; Johnson et al. 2023), snapshot modeling may even be used to reconstruct real-time polarimetric black hole movies of Sgr A*.

Acknowledgments

The Event Horizon Telescope Collaboration thanks the following organizations and programs: the Academia Sinica; the Academy of Finland (projects 274477, 284495, 312496, 315721); the Agencia Nacional de Investigación y Desarrollo (ANID), Chile via NCN19_058 (TITANs), Fondecyt 1221421 and BASAL FB210003; the Alexander von Humboldt Stiftung; an Alfred P. Sloan Research Fellowship; Allegro, the European ALMA Regional Centre node in the Netherlands, the NL astronomy research network NOVA and the astronomy institutes of the University of Amsterdam, Leiden University, and Radboud University; the ALMA North America Development Fund; the Astrophysics and High Energy Physics program by MCIN (with funding from European Union NextGenerationEU, PRTR-C17I1); the Black Hole Initiative, which is funded by grants from the John Templeton Foundation and the Gordon and Betty Moore Foundation (although the opinions expressed in this work are those of the author(s) and do not necessarily reflect the views of these Foundations); the Brinson Foundation; “la Caixa” Foundation (ID 100010434) through fellowship codes LCF/BQ/DI22/11940027 and LCF/BQ/DI22/11940030; Chandra DD7-18089X and TM6-17006X; the China Scholarship Council; the China Postdoctoral Science Foundation fellowships (2020M671266, 2022M712084); Consejo Nacional de Ciencia y Tecnología (CONACYT, Mexico, projects U0004-246083, U0004-259839, F0003-272050, M0037-279006, F0003-281692, 104497, 275201, 263356); the Colfuturo Scholarship; the Consejería de Economía, Conocimiento, Empresas y Universidad of the Junta de Andalucía (grant P18-FR-1769); the Consejo Superior de Investigaciones Científicas (grant 2019AEP112); the Delaney Family via the Delaney Family John A. Wheeler Chair at Perimeter Institute; Dirección General de Asuntos del Personal Académico-Universidad Nacional Autónoma de México (DGAPA-UNAM, projects IN112417 and IN112820); the Dutch Organization for Scientific Research (NWO) for the VICI award (grant 639.043.513), the grant OCENW.KLEIN.113, and the Dutch Black Hole Consortium (with project No. NWA 1292.19.202) of the research program the National Science Agenda; the Dutch National Supercomputers, Cartesius and Snellius (NWO grant 2021.013); the EACOA Fellowship awarded by the East Asia Core Observatories Association, which consists of the Academia Sinica Institute of Astronomy and Astrophysics, the National Astronomical Observatory of Japan, Center for Astronomical Mega-Science, Chinese Academy of Sciences, and the Korea Astronomy and Space Science Institute; the European Research Council (ERC) Synergy Grant

“BlackHoleCam: Imaging the Event Horizon of Black Holes” (grant 610058); the European Union Horizon 2020 research and innovation program under grant agreements RadioNet (No. 730562) and M2FINDERS (No. 101018682); the Horizon ERC Grants 2021 program under grant agreement No. 101040021; the Generalitat Valenciana (grants APOSTD/2018/177 and ASFAE/2022/018) and GenT Program (project CIDEAGENT/2018/021); MICINN Research Project PID2019-108995GB-C22; the European Research Council for advanced grant “JETSET: Launching, propagation and emission of relativistic jets from binary mergers and across mass scales” (grant No. 884631); the FAPESP (Fundação de Amparo à Pesquisa do Estado de São Paulo) under grant 2021/01183-8; the Institute for Advanced Study; the Istituto Nazionale di Fisica Nucleare (INFN) sezione di Napoli, iniziative specifiche TEONGRAV; the International Max Planck Research School for Astronomy and Astrophysics at the Universities of Bonn and Cologne; DFG research grant “Jet physics on horizon scales and beyond” (grant No. FR 4069/2-1); Joint Columbia/Flatiron Postdoctoral Fellowship (research at the Flatiron Institute is supported by the Simons Foundation); the Japan Ministry of Education, Culture, Sports, Science and Technology (MEXT; grant JPMXP1020200109); the Japan Society for the Promotion of Science (JSPS) Grant-in-Aid for JSPS Research Fellowship (JP17J08829); the Joint Institute for Computational Fundamental Science, Japan; the Key Research Program of Frontier Sciences, Chinese Academy of Sciences (CAS, grants QYZDJ-SSW-SLH057, QYZDJ-SSW-SYS008, ZDBS-LY-SLH011); the Leverhulme Trust Early Career Research Fellowship; the Max-Planck-Gesellschaft (MPG); the Max Planck Partner Group of the MPG and the CAS; the MEXT/JSPS KAKENHI (grants 18KK0090, JP21H01137, JP18H03721, JP18K13594, 18K03709, JP19K14761, 18H01245, 25120007, 23K03453); the Malaysian Fundamental Research Grant Scheme (FRGS) FRGS/1/2019/STG02/UM/02/6; the MIT International Science and Technology Initiatives (MISTI) Funds; the Ministry of Science and Technology (MOST) of Taiwan (103-2119-M-001-010-MY2, 105-2112-M-001-025-MY3, 105-2119-M-001-042, 106-2112-M-001-011, 106-2119-M-001-013, 106-2119-M-001-027, 106-2923-M-001-005, 107-2119-M-001-017, 107-2119-M-001-020, 107-2119-M-001-041, 107-2119-M-110-005, 107-2923-M-001-009, 108-2112-M-001-048, 108-2112-M-001-051, 108-2923-M-001-002, 109-2112-M-001-025, 109-2124-M-001-005, 109-2923-M-001-001, 110-2112-M-003-007-MY2, 110-2112-M-001-033, 110-2124-M-001-007, and 110-2923-M-001-001); the Ministry of Education (MoE) of Taiwan Yushan Young Scholar Program; the Physics Division, National Center for Theoretical Sciences of Taiwan; the National Aeronautics and Space Administration (NASA, Fermi Guest Investigator grant 80NSSC20K1567, NASA Astrophysics Theory Program grant 80NSSC20K0527, NASA NuSTAR award 80NSSC20K0645); NASA Hubble Fellowship grants HST-HF2-51431.001-A and HST-HF2-51482.001-A awarded by the Space Telescope Science Institute, which is operated by the Association of Universities for Research in Astronomy, Inc., for NASA, under contract NAS5-26555; the National Institute of Natural Sciences (NINS) of Japan; the National Key Research and Development Program of China (grants 2016YFA0400704, 2017YFA0402703, 2016YFA0400702); the National Science Foundation (NSF, grants AST-0096454, AST-0352953, AST-0521233, AST-0705062, AST-0905844, AST-0922984, AST-1126433, AST-1140030, DGE-1144085, AST-1207704, AST-1207730, AST-1207752, MRI-1228509, OPP-1248097, AST-1310896, AST-

1440254, AST-1555365, AST-1614868, AST-1615796, AST-1715061, AST-1716327, OISE-1743747, AST-1816420, AST-1935980, AST-2034306, AST-2307887); NSF Astronomy and Astrophysics Postdoctoral Fellowship (AST-1903847); the Natural Science Foundation of China (grants 11650110427, 10625314, 11721303, 11725312, 11873028, 11933007, 11991052, 11991053, 12192220, 12192223, 12273022); the Natural Sciences and Engineering Research Council of Canada (NSERC, including a Discovery Grant and the NSERC Alexander Graham Bell Canada Graduate Scholarships-Doctoral Program); the National Youth Thousand Talents Program of China; the National Research Foundation of Korea (the Global PhD Fellowship Grant: grants NRF-2015H1A2A1033752, the Korea Research Fellowship Program: NRF-2015H1D3A1066561, Brain Pool Program: 2019H1D3A1A01102564, Basic Research Support Grant 2019R1F1A1059721, 2021R1A6A3A01086420, 2022R1C1C1005255); Netherlands Research School for Astronomy (NOVA) Virtual Institute of Accretion (VIA) postdoctoral fellowships; Onsala Space Observatory (OSO) national infrastructure, for the provisioning of its facilities/observational support (OSO receives funding through the Swedish Research Council under grant 2017-00648); the Perimeter Institute for Theoretical Physics (research at Perimeter Institute is supported by the Government of Canada through the Department of Innovation, Science and Economic Development and by the Province of Ontario through the Ministry of Research, Innovation and Science); the Princeton Gravity Initiative; the Spanish Ministerio de Ciencia e Innovación (grants PGC2018-098915-B-C21, AYA2016-80889-P, PID2019-108995GB-C21, PID2020-117404GB-C21); the University of Pretoria for financial aid in the provision of the new Cluster Server nodes and SuperMicro (USA) for a SEEDING GRANT approved toward these nodes in 2020; the Shanghai Municipality orientation program of basic research for international scientists (grant no. 22JC1410600); the Shanghai Pilot Program for Basic Research, Chinese Academy of Science, Shanghai Branch (JCYJ-SHFY-2021-013); the State Agency for Research of the Spanish MCIU through the “Center of Excellence Severo Ochoa” award for the Instituto de Astrofísica de Andalucía (SEV-2017-0709); the Spanish Ministry for Science and Innovation grant CEX2021-001131-S funded by MCIN/AEI/10.13039/501100011033; the Spinoza Prize SPI 78-409; the South African Research Chairs Initiative, through the South African Radio Astronomy Observatory (SARAO, grant ID 77948), which is a facility of the National Research Foundation (NRF), an agency of the Department of Science and Innovation (DSI) of South Africa; the Toray Science Foundation; the Swedish Research Council (VR); the US Department of Energy (USDOE) through the Los Alamos National Laboratory (operated by Triad National Security, LLC, for the National Nuclear Security Administration of the USDOE, contract 89233218CNA000001); and the YCAA Prize Postdoctoral Fellowship.

We thank the staff at the participating observatories, correlation centers, and institutions for their enthusiastic support. This paper makes use of the following ALMA data: ADS/JAO.ALMA#2016.1.01154.V. ALMA is a partnership of the European Southern Observatory (ESO; Europe, representing its member states), NSF, and National Institutes of Natural Sciences of Japan, together with National Research Council (Canada), Ministry of Science and Technology (MOST; Taiwan), Academia Sinica Institute of Astronomy and Astrophysics (ASIAA; Taiwan), and Korea Astronomy and

Space Science Institute (KASI; Republic of Korea), in cooperation with the Republic of Chile. The Joint ALMA Observatory is operated by ESO, Associated Universities, Inc. (AUI)/NRAO, and the National Astronomical Observatory of Japan (NAOJ). The NRAO is a facility of the NSF operated under cooperative agreement by AUI. This research used resources of the Oak Ridge Leadership Computing Facility at the Oak Ridge National Laboratory, which is supported by the Office of Science of the U.S. Department of Energy under contract No. DE-AC05-00OR22725; the ASTROVIVES FEDER infrastructure, with project code IDIFEDER-2021-086; and the computing cluster of Shanghai VLBI correlator supported by the Special Fund for Astronomy from the Ministry of Finance in China. We also thank the Center for Computational Astrophysics, National Astronomical Observatory of Japan. This work was supported by FAPESP (Fundacao de Amparo a Pesquisa do Estado de Sao Paulo) under grant 2021/01183-8.

APEX is a collaboration between the Max-Planck-Institut für Radioastronomie (Germany), ESO, and the Onsala Space Observatory (Sweden). The SMA is a joint project between the SAO and ASIAA and is funded by the Smithsonian Institution and the Academia Sinica. The JCMT is operated by the East Asian Observatory on behalf of the NAOJ, ASIAA, and KASI, as well as the Ministry of Finance of China, Chinese Academy of Sciences, and the National Key Research and Development Program (No. 2017YFA0402700) of China and Natural Science Foundation of China grant 11873028. Additional funding support for the JCMT is provided by the Science and Technologies Facility Council (UK) and participating universities in the UK and Canada. The LMT is a project operated by the Instituto Nacional de Astrófisica, Óptica, y Electrónica (Mexico) and the University of Massachusetts at Amherst (USA). The IRAM 30 m telescope on Pico Veleta, Spain, is operated by IRAM and supported by CNRS (Centre National de la Recherche Scientifique, France), MPG (Max-Planck-Gesellschaft, Germany), and IGN (Instituto Geográfico Nacional, Spain). The SMT is operated by the Arizona Radio Observatory, a part of the Steward Observatory of the University of Arizona, with financial support of operations from the State of Arizona and financial support for instrumentation development from the NSF. Support for SPT participation in the EHT is provided by the National Science Foundation through award OPP-1852617 to the University of Chicago. Partial support is also provided by the Kavli Institute of Cosmological Physics at the University of Chicago. The SPT hydrogen maser was provided on loan from the GLT, courtesy of ASIAA.

This work used the Extreme Science and Engineering Discovery Environment (XSEDE), supported by NSF grant ACI-1548562, and CyVerse, supported by NSF grants DBI-0735191, DBI-1265383, and DBI-1743442. The XSEDE Stampede2 resource at TACC was allocated through TG-AST170024 and TG-AST080026N. The XSEDE JetStream resource at PTI and TACC was allocated through AST170028. This research is part of the Frontera computing project at the Texas Advanced Computing Center through the Frontera Large-Scale Community Partnerships allocation AST20023. Frontera is made possible by National Science Foundation award OAC-1818253. This research was done using services provided by the OSG Consortium (Pordes et al. 2007; Sfiligoi et al. 2009), which is supported by the National Science

Foundation award Nos. 2030508 and 1836650. Additional work used ABACUS2.0, which is part of the eScience center at Southern Denmark University. Simulations were also performed on the SuperMUC cluster at the LRZ in Garching, on the LOEWE cluster in CSC in Frankfurt, on the HazelHen cluster at the HLRS in Stuttgart, and on the Pi2.0 and Siyuan Mark-I at Shanghai Jiao Tong University. The computer resources of the Finnish IT Center for Science (CSC) and the Finnish Computing Competence Infrastructure (FCCI) project are acknowledged. This research was enabled in part by support provided by Compute Ontario (<http://computeontario.ca>), Calcul Quebec (<http://www.calculquebec.ca>), and Compute Canada (<http://www.computecanada.ca>).

The EHTC has received generous donations of FPGA chips from Xilinx Inc., under the Xilinx University Program. The EHTC has benefited from technology shared under open-source license by the Collaboration for Astronomy Signal Processing and Electronics Research (CASPER). The EHT project is grateful to T4Science and Microsemi for their assistance with hydrogen masers. This research has made use of NASA's Astrophysics Data System. We gratefully acknowledge the support provided by the extended staff of the ALMA, from the inception of the ALMA Phasing Project through the observational campaigns of 2017 and 2018. We would like to thank A. Deller and W. Brisken for EHT-specific support with the use of DiFX. We thank Martin Shepherd for the addition of extra features in the Difmap software that were used for the CLEAN imaging results presented in this paper. We acknowledge the significance that Maunakea, where the SMA and JCMT EHT stations are located, has for the indigenous Hawaiian people.

ORCID iDs

- Freek Roelofs <https://orcid.org/0000-0001-5461-3687>
 Michael D. Johnson <https://orcid.org/0000-0002-4120-3029>
 Andrew Chael <https://orcid.org/0000-0003-2966-6220>
 Michael Janssen <https://orcid.org/0000-0001-8685-6544>
 Maciek Wielgus <https://orcid.org/0000-0002-8635-4242>
 Avery E. Broderick <https://orcid.org/0000-0002-3351-760X>
 Kazunori Akiyama <https://orcid.org/0000-0002-9475-4254>
 Antxon Alberdi <https://orcid.org/0000-0002-9371-1033>
 Juan Carlos Algaba <https://orcid.org/0000-0001-6993-1696>
 Richard Anantua <https://orcid.org/0000-0003-3457-7660>
 Keiichi Asada <https://orcid.org/0000-0001-6988-8763>
 Rebecca Azulay <https://orcid.org/0000-0002-2200-5393>
 Uwe Bach <https://orcid.org/0000-0002-7722-8412>
 Anne-Kathrin Baczko <https://orcid.org/0000-0003-3090-3975>
 Mislav Baloković <https://orcid.org/0000-0003-0476-6647>
 John Barrett <https://orcid.org/0000-0002-9290-0764>
 Michi Bauböck <https://orcid.org/0000-0002-5518-2812>
 Bradford A. Benson <https://orcid.org/0000-0002-5108-6823>
 Lindy Blackburn <https://orcid.org/0000-0002-9030-642X>
 Raymond Blundell <https://orcid.org/0000-0002-5929-5857>
 Katherine L. Bouman <https://orcid.org/0000-0003-0077-4367>
 Geoffrey C. Bower <https://orcid.org/0000-0003-4056-9982>
 Hope Boyce <https://orcid.org/0000-0002-6530-5783>
 Christiaan D. Brinkerink <https://orcid.org/0000-0002-2322-0749>
 Roger Brissenden <https://orcid.org/0000-0002-2556-0894>
 Silke Britzen <https://orcid.org/0000-0001-9240-6734>
 Dominique Brogiere <https://orcid.org/0000-0001-9151-6683>
 Thomas Bronzwaer <https://orcid.org/0000-0003-1151-3971>
 Sandra Bustamante <https://orcid.org/0000-0001-6169-1894>
 Do-Young Byun <https://orcid.org/0000-0003-1157-4109>
 John E. Carlstrom <https://orcid.org/0000-0002-2044-7665>
 Chiara Ceccobello <https://orcid.org/0000-0002-4767-9925>
 Chi-kwan Chan <https://orcid.org/0000-0001-6337-6126>
 Dominic O. Chang <https://orcid.org/0000-0001-9939-5257>
 Koushik Chatterjee <https://orcid.org/0000-0002-2825-3590>
 Shami Chatterjee <https://orcid.org/0000-0002-2878-1502>
 Ming-Tang Chen <https://orcid.org/0000-0001-6573-3318>
 Yongjun Chen (陈永军) <https://orcid.org/0000-0001-5650-6770>
 Xiaopeng Cheng <https://orcid.org/0000-0003-4407-9868>
 Ilje Cho <https://orcid.org/0000-0001-6083-7521>
 Pierre Christian <https://orcid.org/0000-0001-6820-9941>
 Nicholas S. Conroy <https://orcid.org/0000-0003-2886-2377>
 John E. Conway <https://orcid.org/0000-0003-2448-9181>
 James M. Cordes <https://orcid.org/0000-0002-4049-1882>
 Thomas M. Crawford <https://orcid.org/0000-0001-9000-5013>
 Geoffrey B. Crew <https://orcid.org/0000-0002-2079-3189>
 Alejandro Cruz-Osorio <https://orcid.org/0000-0002-3945-6342>
 Yuzhu Cui (崔玉竹) <https://orcid.org/0000-0001-6311-4345>
 Rohan Dahale <https://orcid.org/0000-0001-6982-9034>
 Jordy Davelaar <https://orcid.org/0000-0002-2685-2434>
 Mariafelicia De Laurentis <https://orcid.org/0000-0002-9945-682X>
 Roger Deane <https://orcid.org/0000-0003-1027-5043>
 Jessica Dempsey <https://orcid.org/0000-0003-1269-9667>
 Gregory Desvignes <https://orcid.org/0000-0003-3922-4055>
 Jason Dexter <https://orcid.org/0000-0003-3903-0373>
 Vedant Dhruv <https://orcid.org/0000-0001-6765-877X>
 Sheperd S. Doeleman <https://orcid.org/0000-0002-9031-0904>
 Sean Dougal <https://orcid.org/0000-0002-3769-1314>
 Sergio A. Dzib <https://orcid.org/0000-0001-6010-6200>
 Ralph P. Eatough <https://orcid.org/0000-0001-6196-4135>
 Razieh Emami <https://orcid.org/0000-0002-2791-5011>
 Heino Falcke <https://orcid.org/0000-0002-2526-6724>
 Joseph Farah <https://orcid.org/0000-0003-4914-5625>
 Vincent L. Fish <https://orcid.org/0000-0002-7128-9345>
 Ed Fomalont <https://orcid.org/0000-0002-9036-2747>
 H. Alyson Ford <https://orcid.org/0000-0002-9797-0972>
 Marianna Foschi <https://orcid.org/0000-0001-8147-4993>
 Raquel Fraga-Encinas <https://orcid.org/0000-0002-5222-1361>
 Per Friberg <https://orcid.org/0000-0002-8010-8454>
 Christian M. Fromm <https://orcid.org/0000-0002-1827-1656>
 Antonio Fuentes <https://orcid.org/0000-0002-8773-4933>
 Peter Galison <https://orcid.org/0000-0002-6429-3872>
 Charles F. Gammie <https://orcid.org/0000-0001-7451-8935>
 Roberto García <https://orcid.org/0000-0002-6584-7443>
 Olivier Gentaz <https://orcid.org/0000-0002-0115-4605>
 Boris Georgiev <https://orcid.org/0000-0002-3586-6424>
 Ciriaco Goddi <https://orcid.org/0000-0002-2542-7743>

- Event Horizon Telescope Collaboration, Akiyama, K., Alberdi, A., et al. 2019a, *ApJL*, **875**, L1, (M87* Paper I)
- Event Horizon Telescope Collaboration, Akiyama, K., Alberdi, A., et al. 2019b, *ApJL*, **875**, L2, (M87* Paper II)
- Event Horizon Telescope Collaboration, Akiyama, K., Alberdi, A., et al. 2019c, *ApJL*, **875**, L3
- Event Horizon Telescope Collaboration, Akiyama, K., Alberdi, A., et al. 2019d, *ApJL*, **875**, L4
- Event Horizon Telescope Collaboration, Akiyama, K., Alberdi, A., et al. 2019e, *ApJL*, **875**, L5
- Event Horizon Telescope Collaboration, Akiyama, K., Alberdi, A., et al. 2019f, *ApJL*, **875**, L6
- Event Horizon Telescope Collaboration, Akiyama, K., Alberdi, A., et al. 2022a, *ApJL*, **930**, L12
- Event Horizon Telescope Collaboration, Akiyama, K., Alberdi, A., et al. 2022b, *ApJL*, **930**, L13
- Event Horizon Telescope Collaboration, Akiyama, K., Alberdi, A., et al. 2022c, *ApJL*, **930**, L14
- Event Horizon Telescope Collaboration, Akiyama, K., Alberdi, A., et al. 2022d, *ApJL*, **930**, L15
- Event Horizon Telescope Collaboration, Akiyama, K., Alberdi, A., et al. 2022e, *ApJL*, **930**, L16
- Event Horizon Telescope Collaboration, Akiyama, K., Algaba, J. C., et al. 2021a, *ApJL*, **910**, L12
- Event Horizon Telescope Collaboration, Akiyama, K., Algaba, J. C., et al. 2021b, *ApJL*, **910**, L13
- Event Horizon Telescope Collaboration, Alberdi, A., Alef, W., et al. 2023, *ApJL*, 957, L20, (M87* Paper IX)
- Gabuzda, D. C., Vitriřchak, V. M., Mahmud, M., & O'Sullivan, S. P. 2008, *MNRAS*, **384**, 1003
- Goddi, C., Martí-Vidal, I., Messias, H., et al. 2021, *ApJL*, **910**, L14
- Gold, R., McKinney, J. C., Johnson, M. D., & Doeleman, S. S. 2017, *ApJ*, **837**, 180
- Hamaker, J. P., Bregman, J. D., & Sault, R. J. 1996, *A&AS*, **117**, 137
- Homan, D. C., Attridge, J. M., & Wardle, J. F. C. 2001, *ApJ*, **556**, 113
- Homan, D. C., & Lister, M. L. 2006, *AJ*, **131**, 1262
- Homan, D. C., & Wardle, J. F. C. 1999, *AJ*, **118**, 1942
- Homan, D. C., & Wardle, J. F. C. 2004, *ApJL*, **602**, L13
- Issaoun, S., Wielgus, M., Jorstad, S., et al. 2022, *ApJ*, **934**, 145
- Janssen, M., Goddi, C., van Bemmél, I. M., et al. 2019, *A&A*, **626**, A75
- Jiménez-Rosales, A., & Dexter, J. 2018, *MNRAS*, **478**, 1875
- Johnson, M. D., Akiyama, K., Blackburn, L., et al. 2023, *Galax*, **11**, 61
- Johnson, M. D., Fish, V. L., Doeleman, S. S., et al. 2015, *Sci*, **350**, 1242
- Johnson, M. D., Lupsasca, A., Strominger, A., et al. 2020, *SciA*, **6**, eaaz1310
- Jones, T. W., & O'Dell, S. L. 1977, *ApJ*, **214**, 522
- Kamruddin, A. B., & Dexter, J. 2013, *MNRAS*, **434**, 765
- Kennett, M., & Melrose, D. 1998, *PASA*, **15**, 211
- Lockhart, W., & Gralla, S. E. 2022, *MNRAS*, **517**, 2462
- Martí-Vidal, I., Roy, A., Conway, J., & Zensus, A. J. 2016, *A&A*, **587**, A143
- Monnier, J. D. 2007, *NewAR*, **51**, 604
- Mościbrodzka, M., Dexter, J., Davelaar, J., & Falcke, H. 2017, *MNRAS*, **468**, 2214
- Mościbrodzka, M., Janiuk, A., & De Laurentis, M. 2021, *MNRAS*, **508**, 4282
- Narayan, R., Iğumenshchev, I. V., & Abramowicz, M. A. 2003, *PASJ*, **55**, L69
- Narayan, R., Palumbo, D. C. M., Johnson, M. D., et al. 2021, *ApJ*, **912**, 35
- Natarajan, I., Deane, R., Martí-Vidal, I., et al. 2022, *MNRAS*, **512**, 490
- Palumbo, D. C. M., & Wong, G. N. 2022, *ApJ*, **929**, 49
- Palumbo, D. C. M., Wong, G. N., & Prather, B. S. 2020, *ApJ*, **894**, 156
- Pearson, T. J. 1999, in ASP Conf. Ser. 180, Synthesis Imaging in Radio Astronomy II, ed. G. B. Taylor, C. L. Carilli, & R. A. Perley (San Francisco, CA: ASP), 335
- Pordes, R., Petravick, D., Kramer, B., et al. 2007, *JPhCS*, **78**, 012057
- Ricarte, A., Johnson, M. D., Kovalev, Y. Y., Palumbo, D. C. M., & Emami, R. 2022a, *Galax*, **11**, 5
- Ricarte, A., Palumbo, D. C. M., Narayan, R., Roelofs, F., & Emami, R. 2022b, *ApJL*, **941**, L12
- Ricarte, A., Prather, B. S., Wong, G. N., et al. 2020, *MNRAS*, **498**, 5468
- Ricarte, A., Qiu, R., & Narayan, R. 2021, *MNRAS*, **505**, 523
- Roberts, D. H., Wardle, J. F. C., & Brown, L. F. 1994, *ApJ*, **427**, 718
- Sfiligoi, I., Bradley, D. C., Holzman, B., et al. 2009, in The Pilot Way to Grid Resources Using glideinWMS, WRI World Congress on Computer Science and Information Engineering, 428
- Smirnov, O. M. 2011, *A&A*, **527**, A106
- Speagle, J. S. 2020, *MNRAS*, **493**, 3132
- Thompson, A. R., Moran, J. M., & Swenson, G. W. J. 2017, Interferometry and Synthesis in Radio Astronomy (3rd ed.; Cham: Springer)
- van Bemmél, I. M., Kettenis, M., Small, D., et al. 2022, *PASP*, **134**, 114502
- Wardle, J. F. C., & Homan, D. C. 2003, *Ap&SS*, **288**, 143
- Wardle, J. F. C., Homan, D. C., Ojha, R., & Roberts, D. H. 1998, *Natur*, **395**, 457
- Wielgus, M., Akiyama, K., Blackburn, L., et al. 2020, *ApJ*, **901**, 67
- Wielgus, M., Marchili, N., Martí-Vidal, I., et al. 2022, *ApJL*, **930**, L19
- Yuan, F., & Narayan, R. 2014, *ARA&A*, **52**, 529